DISSERTATION

Pneumatic tire aquaplaning detection using effect-based methods with a minimal set of sensors

carried out for the purpose of obtaining the degree of Doctor technicae (Dr. techn.)

submitted at TU Wien, Faculty of Mechanical and Industrial Engineering

Dipl.-Ing. Andreas Fichtinger

Mat. Nr.: 00827299

under the supervision of

Ao.Univ.Prof. Dipl.-Ing. Dr.techn. Manfred Plöchl

Institut für Mechanik und Mechatronik, TU Wien

reviewed by

Associate Professor Zsolt SZALAY, Ph.D.

BME Automated Drive Laboratory, Faculty of Transportation Engineering and Vehicle Engineering, Budapest University Of Technology and Economics

and

Univ.Prof. Dipl.-Ing. Dr.techn. Johannes Edelmann

Institut für Mechanik und Mechatronik, TU Wien

Vienna, in March 2024

Doctoral Thesis

I hereby confirm, that the publication of this thesis is subject to the consent of the examination board.

Affidavit

I declare in lieu of oath, that this thesis along with the associated research activities have been acquired by myself, using only the literature cited in this work. Literally cited text passages from different sources have been marked accordingly. I confirm this thesis has never been submitted for examination elsewhere and is in complete agreement with the document assessed by the review committee.

Vienna, March 2024

Andreas Fichtinger

Kurzfassung

Mit aktuellen Entwicklungen im Bereich (teilautonomer) Assistenzsysteme und vollautonomer Fahrzeuge kommt der Informationen zum Thema Fahrbahn-Reifen-Kontakt, speziell des maximalen Reibwerts, zunehmend größere Bedeutung zu. Während der Mensch aufgrund seiner Erfahrungen und bewusster als auch unterbewusster Wahrnehmung die Grenzen für sicheren Betrieb eines Fahrzeugs überwiegend gut einschätzen kann, sind künstliche Systeme vollkommen auf gemessene oder anderwärtig quantifizierte Informationen über den maximalen Reibwert angewiesen. Die laufende Forschung zu diesem Themengebiet befasst sich mit ursachenbasierten und effektbasierten Methoden, welche Informationen über den Reibwert bereitstellen können. Erstere benötigen zusätzliche Sensoren wie z.B. Kameras, Nässesensoren. Effektbasierte Methoden benötigen dazu im Allgemeinen ausreichend hohe Anregung der Reifenkräfte und Fahrzeugreaktionen, um schnell und zuverlässig Reifenparameter, insbesondere den maximalen Reibwert, zu detektieren und auf Änderungen zu reagieren. In alltäglichen Fahrsituationen erreichen die Reifenkräfte in seltenen Fällen die dafür erforderliche Größe, wodurch die Verfügbarkeit einer gültigen Schätzung stark reduziert wird und in vielen Fällen nicht möglich ist.

Es gibt jedoch Effekte welche im Bereich kleiner Radkräfte/schlüpfe einen indirekten Rückschluss auf Änderungen des Reibwerts zwischen Reifen und Fahrbahn ermöglichen. Als Teil dieser Dissertation wird eine Methode zur Schätzung der Schlupfsteifigkeit (Anfangssteigung der Schlupfkurve) und Detektion von Änderungen dieser präsentiert, welche keine explizite, hochgenaue Längsgeschwindigkeit für die Schlupfberechnung benötigt und somit auch für Allradfahrzeuge gut geeignet ist. Zusätzlich wird diese Methode mit einer aktiven Anregung der Reifenlängskräfte kombiniert, um eine persistente Anregung der Eingangsgrößen des Detektionsalgorithmus zu ermöglichen. Dabei werden die Antriebskräfte an beiden Achsen gegengleich variiert, so dass die gewünschte Beschleunigung beibehalten und der Eingriff nicht wahrgenommen wird.

Auf nasser Fahrbahn, welche mit einer durchgehenden Wasserschicht bedeckt ist, kann es, als Spezialfall des Reibwertabfalls, zu Aquaplaning kommen. Beim Verdrängen des Wassers aus dem Reifenlatsch bildet sich eine hydrodynamische Druckverteilung welche die einwirkenden Kräfte auf den Reifen verändert bzw. verschiebt und zu einem (teilweisen) Abheben des Reifens von der Fahrbahn führt. Die maximal übertragbaren Reifenkräfte nehmen mit zunehmender

Fahrgeschwindigkeit und Wasserhöhe ab und gehen schlussendlich gegen null. Das kann in weiterer Folge zu einem Verlust der Steuerbarkeit oder Stabilität des Fahrzeugs führen. Eine Reihe typischer Effekte, die dabei auftreten, erlauben die Detektion von (partiellem) Aquaplaning und werden in dieser Arbeit vorgestellt. Diese sind der charakteristische Spin-Down-Effekt (Verzögerung der Radgeschwindigkeit) an nicht angetrieben Rädern, das Hochdrehen der Reifen an angetriebenen Rädern, erhöhter (Roll-)Widerstand, reduzierte Schlupfsteifigkeit und Änderungen in den Spurstangenkräften. Ergebnisse systematischer Messungen mit variierten Parametern wie Wasserhöhe, Längsgeschwindigkeit, Reifendruck, etc. werden präsentiert und zeigen deren Einfluss auf ausgewählte Aquaplaningeffekte. Im weiteren Teil dieser Arbeit werden Methoden vorgestellt, die unter der Ausnutzung jeweils eines dieser Aquaplaningeffekte (partielles) Aquaplaning detektieren. Als Eingangsgrößen dieser Methoden werden Signale verwendet welche in bestehenden Serienfahrzeugen bereits vorhanden sind bzw. die von der zuvor vorgestellten Methode zur Schlupfsteifigkeitsschätzung berechnet werden. Aufbauend auf den Einzelmethoden werden zwei Detektionsmethoden vorgestellt, welche (partielles) Aquaplaning mit einer Kombination von Kriterien einzelner Aquaplaningeffekte detektieren und somit bedeutend höhere Empfindlichkeit und Robustheit aufweisen.

Abstract

With the recent development of ADAS and fully automated vehicles, information about tire-road contact and especially the friction potential gets more important. While human drivers have a certain feeling for the limits of safe vehicle operation based on their experience and perception, artificial systems completely rely on the quantification of measured or estimated parameters. Ongoing research deals with the detection of road conditions with cause-based methods using additional sensors, e.g. cameras, water sensors, etc., and effect-based methods extrapolating this information from measured vehicle reactions. Effect-based methods usually require persistent excitation of forces, accelerations, etc., to rapidly and reliably detect friction parameters and adapt to their changes. Common driving maneuvers in public traffic rarely exhibit necessary levels and changes of tire force and vehicle reaction, reducing the availability of these parameters or making their determination even impossible.

However, certain effects influencing low slip tire behavior allow an indirect detection of changes in tire-road friction even for small longitudinal tire forces. Part of this dissertation is a method estimating tire slip stiffness (initial slip slope) and its changes, especially for all-wheel drive cars, where an explicit longitudinal velocity for slip calculation might not be available. This method is combined with an active excitation of longitudinal tire forces, in a way that persistent excitation needed for the algorithm is generated. The forces on both axles are slightly varied, while their sum is kept at the level to maintain the desired vehicle acceleration and the intervention is not recognized.

During wet road conditions, if the water on the road forms a continuous layer, aquaplaning can occur as a special case of friction potential reduction. The tire squeezes the water out of its contact area, resulting in a hydrodynamic pressure distribution altering the tire forces and (partially) lifting the tire from the ground. This results in a reduction of friction potential with increasing velocity and water height, which eventually leads to a total loss of tangential tire forces and therefore loss of controllability or stability. Several typical effects that come along with (partial) aquaplaning allow its detection and are presented in this paper. These are the unique spin-down effect on non-driven tires, spin-up on driven tires, increased rolling resistance, reduced slip slope and tie rod force changes on front tires. Water level height, longitudinal velocity, tire pressure, and several other parameters relevant for aquaplaning are varied and their influence on chosen effects is investigated. Based on the findings, detection

algorithms for these single effects are developed using basic measurement signals available in series production cars and the previously presented slip slope detection method. Eventually, two joint algorithms using criteria and output from the single methods are presented detecting (partial) aquaplaning in various driving situations.

Preface

Auch wenn am Titelblatt zuallererst und am größten der Name des Dissertanten prangt, so ist eine derart umfassende Arbeit niemals nur die Leistung einer Person, sondern vielmehr das Ergebnis der Zusammenarbeit und dem Austausch von vielen Unterstützern im Fachlichen wie auch Persönlichem. So ist es natürlich auch im Falle meiner Dissertation und ich möchte in den folgenden Zeilen, ohne Anspruch und Garantie auf Vollständigkeit, einigen der Personen die mich auf diesem Weg begleitet und unterstützt haben danken.

Zuallererst ist hier natürlich der Initiator dieser Arbeit, mein Dissertationsbetreuer Professor Dr. Manfred Plöchl zu nennen, der mich überzeugt hat, sich dieser Aufgabe zu stellen. In gleichem Atemzug muss ich auch Prof. Dr. Johannes Edelmann nennen, welcher in gleichem Maße immer Teil dieser Dissertation war. Gemeinsam sind sie immer zu jeder Frage mit Rat und Tat zur Seite gestanden, haben interessante Denkanstöße gebracht und die richtigen Fragen gestellt um es mir zu ermöglichen, ein tieferes Verständnis der Fahrzeugdynamik und Mechanik aufzubauen. Abseits der fachlichen Zusammenarbeit bleiben mir aber auch die vielen gemeinsamen Abendessen mit dem einen oder anderen Gläschen Wein und unsere gemeinsamen Fahrdynamikerprobungen in guter Erinnerung.

Eine wichtige Rolle in der Zeit als Dissertant haben meine Kolleginnen und Kollegen eingenommen, welche, so wie ich, denselben Weg hinein ins Doktorat an der Uni eingeschlagen haben. Da gab es einerseits die „alten Hasen“: Martin Haudum, Julia Blabensteiner und Florian Klinger, zu denen ich als Neuling in der Universitätswelt dazu gestoßen bin und herzlich aufgenommen wurde. Insbesondere möchte ich Martin danken, für viele Stunden Unterstützung bei der Entwicklung der Simulationsumgebung und beim Aufbau der Messtechnik für die praktischen Fahrversuche welche vieles deutlich einfacher gemacht oder überhaupt erst ermöglicht haben.

Besonders gerne denke ich an die gemeinsame Zeit mit meinen beiden ehemaligen Zimmerkollegen Christian Pittner und Florian Zehetbauer zurück, mit denen ich wohl die längste gemeinsame Zeit am Institut verbracht habe und viele fachliche wie auch persönliche Gesprächen geführt und auch so manches gute Mittagessen gemeinsam zubereitet habe.

Und dann möchte ich noch besonders „die Jungen“, Bernhard Ebner und Philipp Mandl, erwähnen, welche gegen Ende meiner Zeit am Institut viel Schwung und Abwechslung in den Alltag gebracht haben.

Natürlich gilt mein Dank auch alle anderen Institutsangehörigen, aus der eigenen und den anderen Arbeitsgruppen, wobei ich hier noch insbesondere Prof. Heinz-Bodo Schmiedmayer, Prof. Eray Arslan, Elisabeth Hansy-Staudigl, Jakob Scheidl und Christian Schmidrathner nennen möchte.

Grundsätzlich ermöglicht wurde die Dissertation erst durch die Finanzierung der Assistentenstelle aber auch Zurverfügungstellung von umfangreicher Unterstützung durch den Projektpartner Porsche AG. Besonderer Dank hierfür gilt Dr. Manfred Harrer, welcher den Beginn dieser Finanzierung ermöglicht hat, Manuel Höll, der als enger Ansprechpartner diese Forschungspartnerschaft durch die ganzen Jahre begleitet hat, sowie Michael Unterreiner und Florian Büttner für die langjährige gute Zusammenarbeit und erfolgreiche gemeinsame Erprobungen.

Große Teile dieser Arbeit entstanden in Kooperation mit den geschätzten Kollegen Prof. Zsolt Szalay und Ádám Bárdos von der Technischen Universität Budapest. Danke für die gute Zusammenarbeit, köszönöm szépen a jó együttműködést!

Speziellen Dank möchte ich hier zwei sehr engen und guten Freunden, Markus Röglsperger und Magdalena Dainko, aussprechen, welche in all den Jahren an der Uni (und auch davor) ein offenes Ohr für meine Freuden als auch Sorgen hatten und mir geholfen haben bei unzähligen Spielabenden und Gläschen Wein die nötige Ablenkung vom Dissertationsalltag zu finden.

Allergrößter Dank gilt jedoch meinen Eltern, Aniela und Gerhard, ohne deren Unterstützung und Aufopferung ich es niemals diesen Weg gehen und erfolgreich abschließen hätte können! Danke!

Contents

Chapter 1

Introduction

Tire-road contact behavior is one of the main factors influencing vehicle dynamics. Knowledge about the current road condition, in particular about the currently achievable maximum tire forces, contributes a major part to vehicle safety. Various road conditions such as snow, ice, water layers that may cause aquaplaning, etc. change the tire contact behavior and require the human driver or autonomous system to adapt for safe operation of the vehicle, e.g. lower cornering speed or larger distance to vehicles in front. Changes in these conditions, e.g. during heavy showers of rain or snow and when changing to another lane or road, require a permanent reevaluation and monitoring of the new situation. The underlying phenomena determining the tire contact behavior, its maximum forces, and their reduction differ depending on the specific road surface. On solid and dry surfaces tire-road contact is dominated by adhesion and material hysteresis, [1], [2]. On snow and ice or at combinations of these and on other layers like gravel additional phenomena occur and depend more on additional parameters, e.g. temperature, [1] [3] [4]. If the road surface is covered with a constant water layer, additionally to rubber-road contact hydrodynamic processes in the tire contact patch alter the force distribution. While human drivers (usually) adapt their driving on their perception and experience, but may also profit from additional information, ADAS and (semi)autonomous systems rely completely on the quantification of the road conditions, especially the maximum possible tire forces or safe driving velocity. With further implementation of such systems in series production cars and the future goal of fully autonomous driving systems, the focus is increasingly directed to methods for tire-road friction determination. These are generally distinguished into two categories: cause- and effect-based methods, [5]. Cause-based methods usually require additional sensors, e.g. cameras, moisture sensors, etc., and additional signal and data processing for extrapolation of their measurements to tire-road friction potential. They are especially beneficial because they allow the determination of road conditions independent of the vehicle and its current state and may also have capabilities to determine road

conditions ahead of the vehicle. Effect-based methods determine the tire-road contact characteristics based on the reaction of the vehicle or its tires to current road conditions and vehicle states. However, reliable determination of the friction potential is difficult in normal driving situations. Estimation of the maximum friction coefficient based on longitudinal dynamics requires at least 60% utilization of the friction potential on dry surfaces and even more on low-friction surfaces [6]. Lateral dynamics may allow for earlier detection if pneumatic aligning torques are used for friction coefficient estimation [7] [8] [9] [10]. These show earlier nonlinear behavior that allows the determination of the maximum friction coefficient at lower slip values. Precise determination of pneumatic aligning torques may however be difficult in practical application and sensitive to errors in measurements and modeling. Despite slip stiffness is described as a pure tire parameter [11], independent of the maximum friction potential, several publications describe a correlation between friction potential drop and changes in the initial slip slope. [12] proposed slip slope as a feasible measure to detect critical road conditions and warn the driver. Possible explanations of the reduced slip slope are given in [5] [13] [14]. One influencing factor is a certain compliance of road surfaces like snow, ice, or gravel, which acts in series with the tire bristle stiffness and leads to a lower initial slip slope. Besides that, [14] describes rolling resistance and existing longitudinal stress distribution in the free-rolling tire as additional effects, which are directly related to the maximum friction coefficient, but have only a minor impact on the initial slip slope. To detect friction coefficient changes [14] uses a recursive least square parameter identification method to detect slip slope from slip and normalized traction force. [15] proposed a linear Kalman filter with a change detection for direct estimation of slip slope and a slip-offset parameter on a two-wheel driven vehicle. Additionally, a texture measure based on the variance of the difference between vehicle velocity and wheel speeds was used to distinguish between different low friction surfaces with similar slip slope levels. [16] developed a nonlinear tire model for joint estimation of slip slope and maximum friction coefficient with an extended Kalman filter. [17] used a linear tire model and an RLS method for slip slope estimation and a linear relation between slip slope and maximum friction coefficient.

All slip slope estimation approaches have in common that actual slip has to be calculated accurately and therefore, require a high-quality longitudinal (wheel) velocity signal. For two-wheel driven vehicles the wheel speed signal of the free-rolling tires can be used as reference velocity. An advantage of using wheel speeds for reference velocity determination is that these are permanently available and signal processing is the same. There is no additional time delay or other differences from different measurement systems or signal processing transfer functions which may reduce quality. For all-wheel

drive vehicles or braking, however, no direct measurement of the vehicle speed is available without additional sensors, e.g. GPS, or additional estimation methods for the longitudinal velocity, [18] [19] [20]. Another possible solution [21] describes a slip slope estimator that can be used for all-wheel drive vehicles using differences in wheel speeds and traction coefficients between the two axles.

As mentioned above, a special case of tire-road friction potential reduction is aquaplaning, which occurs on wet roads covered with a continuous water layer. Early aquaplaning research [22] [23] identified a couple of (unique) phenomena that can occur under these conditions. The tire tread penetrates the water layer and displaces not all water out of the contact patch area, which causes hydrodynamic pressures. The water forms a wedge at the front of the tire contact patch, alters the (vertical) stress distribution and therefore the resulting forces. This operating state of the tire is called partial aquaplaning, as long parts of the tire contact patch are still in (dry) contact with the road surface. The size of the tire contact patch in dry contact with the road surface decreases with increasing velocity or water layer thickness. If the remaining contact eventually vanishes completely, the tire lifts off the ground and the vertical tire forces are then generated by the hydrodynamic forces, which is referred to as total aquaplaning. In contrast to solid surfaces, e.g. snow, ice, or gravel, a total loss of longitudinal and lateral friction potential occurs in this case, which might cause a loss of controllability or stability of the vehicle. The hydrodynamic pressure distribution in the tire contact patch shifts the resulting vertical force to the front, causing increased rolling resistance.

On non-driven wheels, this leads to a unique phenomenon occurring at (close to) total aquaplaning, called spin-down. The rolling resistance exceeds all other remaining forces and torques, causing to rapidly decelerate the wheel speed, which can even lead to a full stop of the tire. Driven wheels may spin up if the driving torque exceeds the maximum residual traction potential and the rolling resistance. Several publications have used optical [24] and acceleration [25] [26] [27] sensors that measure the contact patch length of the tire, allowing early detection of partial aquaplaning. Acceleration sensors are mounted on the inner liner of the tire, optical sensors consist of two parts, one on the inner liner and an additional one on the rim. On the one hand, robustness against high loads, wide temperature ranges, and aging of the sensors is important for reliable detection, on the other hand, the strength and durability of the tire as a critical part for safety must not be weakened. These requirements make tire sensors still very cost-intensive and therefore they are not implemented in series production yet. [28] indicated that partial aquaplaning causes the slip slope to drop and [29] explained it with the decreasing contact length of the tire tread. Therefore, slip slope drop can

give an early indication of partial aquaplaning and allows a limited quantification of the expected full aquaplaning velocity, making slip slope estimation an important part of aquaplaning detection. Several other effect-based approaches for the detection of aquaplaning have been patented, usually focusing on single aquaplaning phenomena or driving situations. Many of these approaches rely on additional sensors to detect water spray, e.g. [30], [31]. Others use readily available measured signals used by ABS or ESC control. [32] used wheel speed signals to determine critical deceleration levels and slips for detection of aquaplaning spin-downs with and without braking. An approach for aquaplaning detection was presented in [33] and [34] based on a comparison of the actual measured wheel speed signals at the front tires with a stored reference. Bumps and rough terrain that may also cause spin-down like wheel speed signals are excluded from detection by comparing the wheel speed signal pattern of the front and rear wheels passing the same point. [35] used the measured wheel speed signals to analyze changes in high-frequency rotational oscillation of the tire caused by the reduction of the contact length to identify aquaplaning. [36] calculates the resistance from displacing the water at the tires with a longitudinal vehicle model using measured acceleration, road grade, longitudinal tire forces, and nominal rolling and aerodynamic drag resistance parameters. These effect-based approaches have in common that they are generally based on a single aquaplaning phenomenon.

1.1. Scope of the thesis

To this point, known aquaplaning detectors focus on single effects and corresponding methods. The goal of the papers comprising this thesis is to develop a joint algorithm for aquaplaning detection based on a set of aquaplaning phenomena, without the use of additional sensors. The algorithm allows for aquaplaning detection during more driving situations and a higher sensitivity than single-effect methods. As a basis for the algorithm developed, Paper (2) presents results of measured effects from the tire and from the vehicle that are useful for detection within a series production car. These effects may occur before (increased rolling resistance, slip slope change), close to (minor wheel spin-downs), or at full aquaplaning (wheel spin-ups/downs, tie rod force changes) at a tire. Measurements are compared for several parameter variations like water level, velocity, drive train concept, tire type, wear, and pressure. Especially slip slope changes give early information about changes in the surface condition on low friction surfaces, like ice and snow, and during (partial) aquaplaning. For calculation of the longitudinal tire slip high-quality velocity information is necessary which makes reliable slip slope

detection difficult, for all-wheel drive cars. Therefore, in Paper (3) a method is presented that allows slip slope estimation on all-wheel (and two-wheel) drive vehicles without the need for an explicit longitudinal velocity for slip calculation. It can detect slip slopes for different nominal tire parameters on both axles and can adapt to changes in these during operation. Additionally, a new active longitudinal force excitation for all-wheel drive is suggested to increase the availability of the estimated slip slope signal. The individual tire forces are varied on both axles while keeping their sum constant and therefore not changing the current vehicle acceleration. Paper (1) describes algorithms to detect some of the aquaplaning effects individually that were presented in Paper (2), with a special focus on rear-wheel drive cars. A novel method for the detection of minor short-time spin-downs on front wheels is presented, using moving variance measures of wheel accelerations. Based on single-effect methods two joint algorithms are presented that detect (partial) aquaplaning and can warn the driver or (semi)autonomous systems. The first joint algorithm combines the key criteria and the outputs from the single effect-based methods. Increased rolling resistance is used as a robust standalone detection, but also as a necessary criterion for the detection of other phenomena. The second joint algorithm combines the outputs from the single methods, based on the change detection method, to a joint aquaplaning measure.

1.2. List of publications and contribution

This thesis consists of a summary of the addressed topics and the following four appended papers:

1. Fichtinger, A., Edelmann, J., Plöchl, M., Höll, M. *Aquaplaning Detection Using Effect-Based Methods: An Approach Based on a Minimal Set of Sensors, Electronic Stability Control, and Drive Torques*. IEEE Vehicular Technology Magazine 16.3 (2021): 20-28.
   Andreas Fichtinger is responsible for: writing the original draft; development and implementation of the proposed single and joint detection methods; preparation and planning of the measurements; testing of the method with simulated and measured data

2. Fichtinger, A., Bárdos, Á., Szalay, Z., Edelmann, J., Plöchl, M. *Pneumatic tyre aquaplaning: an experimental investigation on manifestations and influences of appearance*. Acta Polytechnica Hungarica 19.9 (2022): 45-65.
   Andreas Fichtinger is responsible for: writing the chapters about resistance, slip slope, and tie rod force effects of the original draft; evaluation of measurement data; preparation and planning of the tests with the AWD and one RWD vehicle

3. Fichtinger, A., Edelmann, J., Plöchl, M., Höll, M., Unterreiner, M. *Slip Slope Change Detection Based on Active Drive Force Excitation*. Proceedings of the Institution of Mechanical Engineers. Part D, Journal of Automobile Engineering (2023), Web.
   Andreas Fichtinger is responsible for: writing the original draft; the development of the active excitation method; implementation of the proposed estimation and active excitation methods; sensitivity analysis of the estimation method; preparation and planning of the measurements; testing of the method with simulated and measured data

4. Fichtinger, A., Edelmann, J., Plöchl M. (2022). *Tire-road friction potential estimation for all-wheel drive vehicles with active longitudinal tire force excitation*. In Proceedings of AVEC. Vol. 2022.
   Andreas Fichtinger is responsible for: writing the original draft; the implementation of the simulation; sensitivity analysis of the active excitation method; planning of the test maneuvers; test of the method with measured data

Chapter 2

Aquaplaning phenomena and detection algorithms

On wet road surfaces with a continuous water layer, aquaplaning may occur as a special case of reduction of tire-road friction. Water is squeezed out between the tire treads and road surface, forming a water wedge that lifts the tire contact patch at its front. This area at the tire contact patch grows with increasing velocity and water height, Figure 2.1, and is dependent on various tire and road parameters. The hydrodynamic pressure distribution in the area of the water wedge alters the position of the resulting vertical tire force and increases rolling resistance. At the same time the tire tread, which is separated from the road surface by the water wedge, cannot generate tangential forces reducing the maximum longitudinal and lateral forces of the tire. This situation is further referred to as partial aquaplaning, [23]. Full aquaplaning occurs if the remaining tire contact patch in dry contact with the road vanishes and the hydrodynamic pressure distribution generates the entire vertical tire force. Hence, the tire cannot generate any longitudinal or lateral forces. On non-driven front wheels total aquaplaning leads to a loss of controllability while on non-driven rear tires, a loss of stability of the vehicle occurs. In the case of driven wheels, the loss of stability or controllability can occur even under partial aquaplaning conditions if the applied longitudinal forces exceed the maximum residual friction potential.

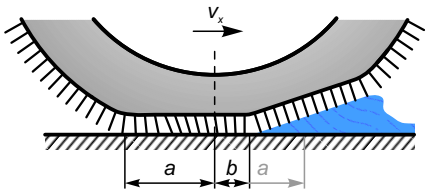

Figure 2.1.: Tire contact at wet road conditions with reduced contact patch length

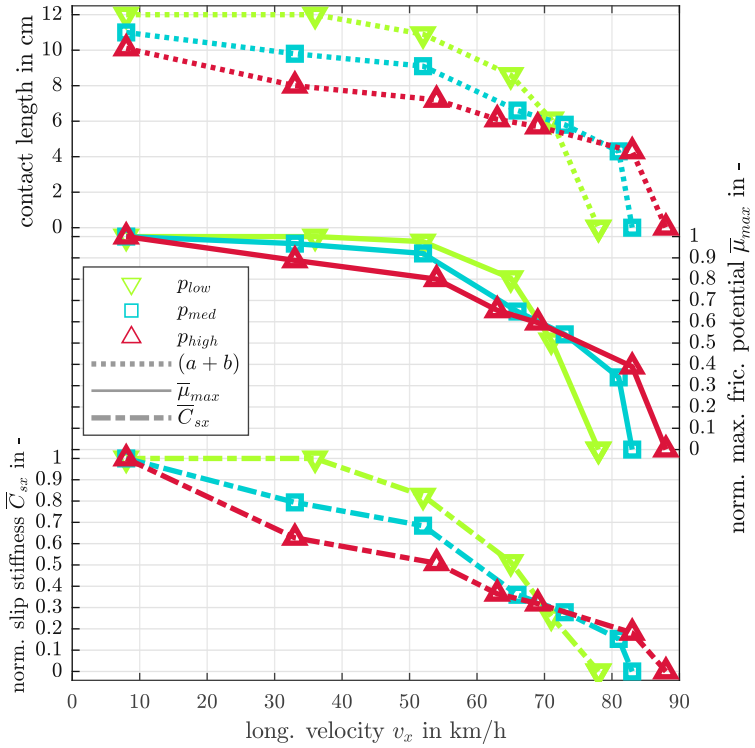

Figure 2.2.: Tire contact length measured with inner liner tire sensors from [37]. Calculated normalized maximum traction coefficient and slip slope.

The reduction of the tire contact patch length in dry contact was measured in [37] with tire sensors for three different inflation pressures, Figure 2.2 top. Based on these contact patch lengths, the middle plot shows the normalized maximum friction coefficient calculated using the Brush tire model, equation (2.1), from [11]. Figure 2.2 bottom shows the expected normalized slip stiffness of the tire, also calculated from the Brush tire model, Equation (2.2). These calculated curves indicate that slip stiffness can be useful as an early indicator for partial aquaplaning, given its quadratic dependence on the remaining tire contact patch length in contact.

$$F_{x,\max} = \frac{(2a-b)\,(a+b)^2\,F_z\mu}{4a^3} \quad \rightarrow \quad \mu_{\max} = \frac{F_{x,\max}}{F_z} \tag{2.1}$$

$$F_x = \frac{1}{2}c_{px}\,(a+b)^2\,s_x \quad \rightarrow \quad C_{sx} = \frac{\partial F_x}{\partial s_x}|_{s_x=0} = \frac{1}{2}c_{px}\,(a+b)^2 \tag{2.2}$$

Experimental measurements of the residual maximum traction coefficient and the slip stiffness are shown in the corresponding sections for spin-up and slip slope, Sections 2.1 and 2.3. Other typical aquaplaning phenomena presented in the following sections

and used for detection of (partial) aquaplaning are the characteristic spin-down of non-driven tires, increased rolling resistance, and changes in the tie rod forces.

2.1. Spin-Down and Spin-Up

At full aquaplaning, a tire does not generate tangential forces and the resulting vertical force from hydrodynamic pressure is shifted to the front of the tire, increasing the rolling resistance. On a non-driven wheel, no torque acts against this increased resistance force and the wheel speed decreases rapidly causing a spin-down that can even cause the tire to stop turning. Measurements have shown that even before full aquaplaning very short minor spin-downs occur, giving an early indication of (partial) aquaplaning. Figure 2.3 shows vehicle velocity and wheel speed signals of an RWD vehicle with worn summer tires during constant velocity passes over a watered asphalt lane with approximately 1.3 mm water level height. All maneuvers are aligned along the time axis so that the watered lane starts at 1 s. At approximately 89 km/h some minor spin-downs of the front right and left wheels can be seen shortly after 2 s and at 3 s. With increasing velocities, 98 km/h and 106 km/h, the number and magnitude of the spin-downs increase but the vehicle is still controllable and stable. At a velocity of approximately 118 km/h the front right wheel spins down immediately after entering the watered lane and the maneuver was aborted due to a simultaneous spin-up of the rear tires. Figure 2.4 shows the corresponding slip values over velocity for these maneuvers. The pale color data points show slip values for additional maneuvers (constant velocity and accelerated) with the same tires and water level heights that are not shown in the time plot. The distribution of the data points shows clearly that minor spin-downs occur even 20 km/h below the actual full aquaplaning velocity and are a good indication for (partial) aquaplaning. Detecting these allows for a reaction before reaching full aquaplaning speed. Measurements with new winter tires did not show these minor spin-down events.

If (partial) aquaplaning builds up at driven wheels, the residual maximum traction coefficient correlates with the tire contact patch length in dry contact, Equation (2.1). Additionally, the driving torque has to act against the increased rolling resistance. Contrary to spin-downs, spin-ups can occur at velocities far below total aquaplaning speed depending on the actual drive torque at the tire, if its value is larger than the maximum residual traction forces and the increased rolling resistance. Figure 2.5 and 2.6 show the irregular occurrence of spin-ups referred to velocity at the rear tires of a RWD car. However, residual maximum traction coefficients at spin-ups decrease with

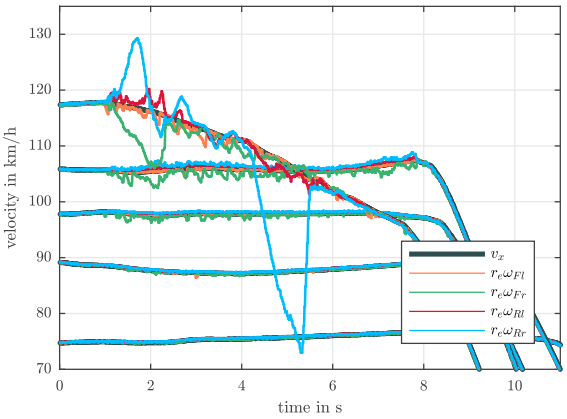

Figure 2.3.: Wheel speed signals at different velocities with full and partial aquaplaning. Minor spin-downs occur approximately 20 km/h below full aquaplaning speed. Worn summer tires with low inflation pressure at a water level height of 1.3 mm.

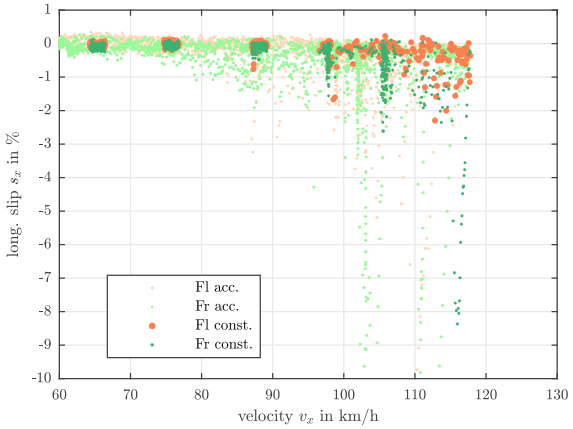

Figure 2.4.: Wheel slip at front tires over velocity during full and partial aquaplaning showing exponential behavior. Worn summer tires with low inflation pressure at a water level height of 1.3 mm.

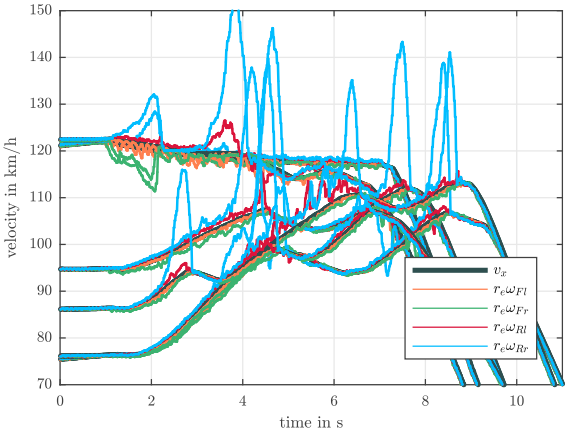

Figure 2.5.: Wheel speed signals at different velocities with full and partial aquaplaning. Spin-ups at rear tires occur at different velocities depending on the current tire force. Worn summer tires with high inflation pressure at a water level height of 1.3 mm.

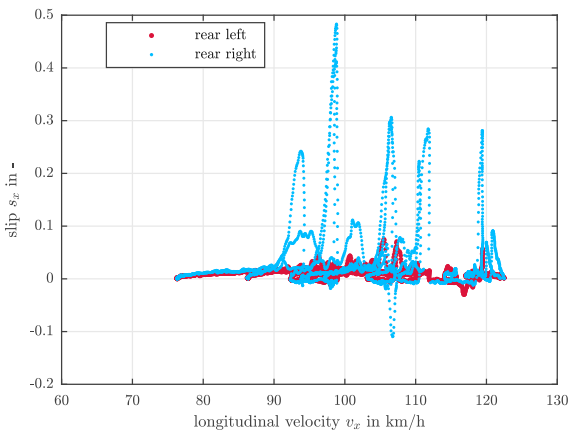

Figure 2.6.: Wheel slip at rear tires over velocity during full and partial aquaplaning spin-ups. Worn summer tires with high inflation pressure at a water level height of 1.3 mm.

increasing velocity as described by Equation (2.1) and Figure 2.2, middle. The average actual traction coefficients during spin-ups within particular velocity ranges are plotted in Figure 2.7 for the rear left and right tires. Traction coefficient curves from the left and right wheels differ because of a significantly lower and more irregular water level height on the left side of the lane.

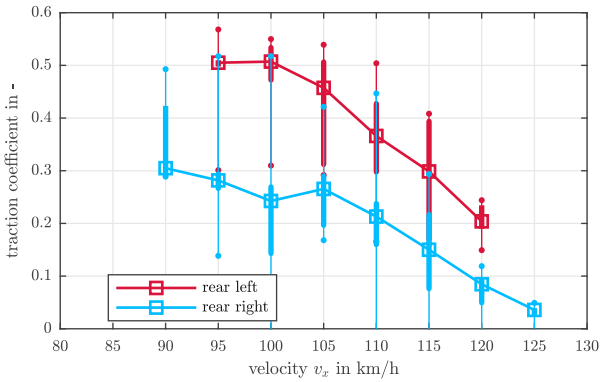

Figure 2.7.: Actual traction coefficient at driven rear-wheel tires during spin-ups within finite ranges of vehicle velocity. Worn summer tires with high inflation pressure at a water level height of 1.3 mm.

Detection algorithms

Large spin-up and spin-down events at (partial) aquaplaning cause wheel speeds and accelerations to be (much) higher or lower than the current vehicle speed and acceleration. Hence, the difference between wheel and vehicle accelerations allows to detect such events:

$$a_{w,\Delta,i} = \dot{\omega}_i r_{ei} - a_x \tag{2.3}$$

Similar negative acceleration differences may occur during a spin-down or at the end of a spin-up when the wheel decelerates before it reaches the same level as vehicle speed again. The same applies to spin-ups and the end of spin-downs. Hence, the sign of the wheel and vehicle speed difference is used additionally for the distinction of these situations:

$$v_{w,\Delta,i} = \omega_i r_{ei} - v_x \tag{2.4}$$

To increase robustness the acceleration difference is not evaluated directly but used to calculate a cumulative sum for detection, similar to the CUSUM change detection algorithm, [15]. Spin-up detection is additionally limited to actual traction coefficients less than 0.07 to avoid misdetection of spin-ups on other low-friction surfaces. Figure 2.8 shows the wheel and vehicle speeds during a maneuver with spin-ups and spin-downs on different wheels, the corresponding acceleration differences, and the (down-sampled) output of the detection algorithm.

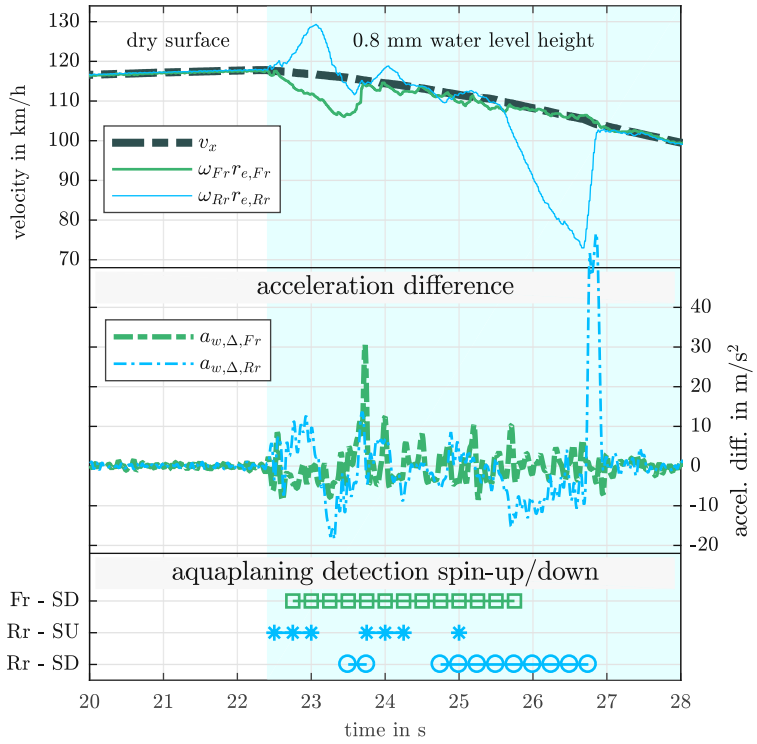

Figure 2.8.: Wheel spin-down and spin-up detection during full aquaplaning on non-driven front right and driven rear right wheel based on acceleration differences between wheels and vehicle. Worn summer tires with low tire pressure and an average water level height of 0.8 mm.

Depending on its parameterization as well as the magnitude and duration of the spin-downs, the previous algorithm may not detect upcoming aquaplaning. Analysis of measurement data reveals that small spin-downs can occur on non-driven tires at velocities up to 20 km/h below full aquaplaning speed, Figure 2.3. Again, for calculation of the aquaplaning indicator acceleration difference between wheel and vehicle is used, Equation (2.3). Instead of evaluating it directly, the exponentially weighted moving variance, [38], is calculated and used for detection:

$$\overline{\Delta a}_{x,i,k} = (1-\alpha)\,\overline{\Delta a}_{x,i,k-1} + \alpha\,\Delta a_{x,i,k} \tag{2.5}$$

$$\sigma^2_{\omega,\Delta,i,k} = (1-\beta)\left(\sigma^2_{\omega,\Delta,i,k-1} + \beta\,(\Delta a_{x,i,k} - \overline{\Delta a}_{x,i,k-1})^2\right) \tag{2.6}$$

$$\text{mit} \quad i = Fl, Fr, Rl, Rr \tag{2.7}$$

Absolute levels of the variance measures can vary for different tires and especially on different grounds and other low friction surfaces, e.g. gravel, rough snow. However,

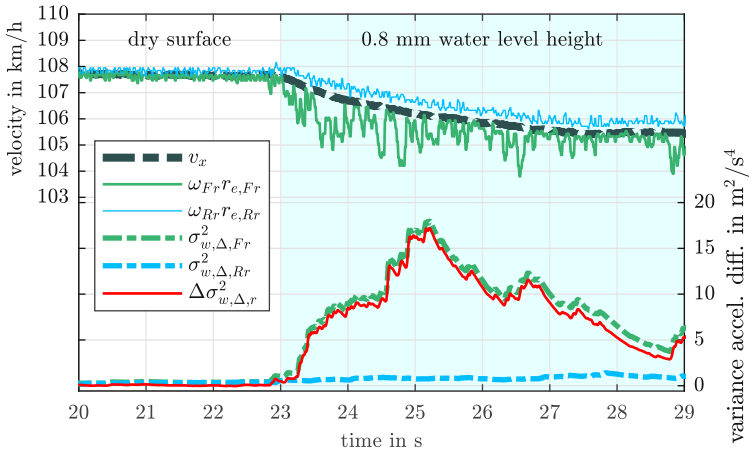

Figure 2.9.: Detection of minor spin-downs on non-driven front wheel based on differential variance measure of wheel accelerations during a maneuver with almost constant velocity. Worn summer tires with low tire pressure and an average water level height of 0.8 mm.

minor spin-downs usually just occur at one (non-driven) axle. Hence, the differences of the variance between the front and rear tires at each vehicle side are used to evaluate for aquaplaning:

$$\Delta\sigma^2_{\omega,\Delta,j} = \sigma^2_{\omega,\Delta,Fj} - \sigma^2_{\omega,\Delta,Rj} \quad \text{mit} \quad j = \text{left, right} \tag{2.8}$$

Figure 2.9, top plot, shows the wheel speeds of the right vehicle side in comparison with the absolute longitudinal vehicle velocity on an RWD vehicle. At 23 s the vehicle enters the watered lane and a series of minor spin-downs starts immediately at the front wheel, while the rear wheel only has a slightly increased slip. The bottom plot shows the exponentially weighted moving variance measures of the front and rear wheels as dash-dotted lines and the difference between those as solid red line. The front wheel variance measure shows a strong increase shortly after the beginning of the watered lane while the rear variance only slightly changes, resulting in a variance difference that follows the front wheel variance and clearly indicates aquaplaning.

2.2. Rolling resistance

The hydrodynamic processes in the tire contact patch cause an increase in rolling resistance, which depends on several factors, mainly water level height and vehicle velocity, [23]. Since individual tire rolling resistance measurement would require additional sensors, the change of total (rolling) resistance of the whole vehicle compared to dry,

solid surfaces is suggested as a practical measure. Similar to [36], measured acceleration from the ESC is compared to a calculated, nominal acceleration based on vehicle mass, nominal tire rolling resistance, aerodynamic drag coefficient, and current drive torque to detect changes in resistance. Therefore, the difference between measured and calculated acceleration serves as an indicator for the rolling resistance change:

$$\Delta a_x = a_{x,\text{nom}} - a_{x,\text{meas,ESC}} \tag{2.9}$$

For calculation of the nominal acceleration $a_{x,\text{nom}}$ wheel torques T_i and basic vehicle parameters are necessary. With these parameters and inputs, the acceleration is calculated using the following form:

$$a_{x,\text{nom}} = \frac{1}{m}\left(\sum_{i=1}^{4}\left(\frac{T_i}{r_{l,i}} - r_{w,i}F_{z,i}\right) - c_x v_x^2\right) \tag{2.10}$$

with vehicle mass m, nominal rolling resistance coefficient $r_{w,i}$, aerodynamic drag constant $c_x\,(=\,1/2\,c_w A\rho)$, and the loaded wheel radius $r_{l,i}$. Especially mass and nominal rolling resistance are important, can change during normal operation, and therefore have to be determined under dry conditions using a separate estimator, [39] [40].

Figure 2.10 shows a time plot of this resistance measure for a constant velocity maneuver with a change from dry asphalt to a water-covered lane. Averaged values of the resistance measure are shown over velocity in Figures 2.11 to 2.15 for varying velocity, water height, and different tire parameters. For all tested tire and parameter combinations resistance increases with vehicle velocity. There is no significant change in the level and gradient of the resistance measure for low water level height (0.6 - 1.3 mm), Figure 2.11. However, at 2 mm water level height the resistance and its velocity gradient increase significantly. New or deep tire treads, e.g. on winter tires and new summer tires, are subjected to a (much) lower increase of rolling resistance and its gradient than worn summer tires, Figures 2.12 and 2.13. Despite the actual aquaplaning speed depends on tire inflation pressure, it has no significant influence on the rolling resistance change for low water level heights (1.3 mm), Figure 2.14. In general, an increase of resistance by at least 0.2 m/s^2 is a good threshold for the identification of partial aquaplaning with the tested vehicle and tire combinations, as the resistance measure plots show. The final figure shows a combined comparison of tire pressure and a load variation between the front and rear axle. An additional weight of approximately 270 kg was added to the front or close to the rear axle and tire pressure was varied from low to medium tire

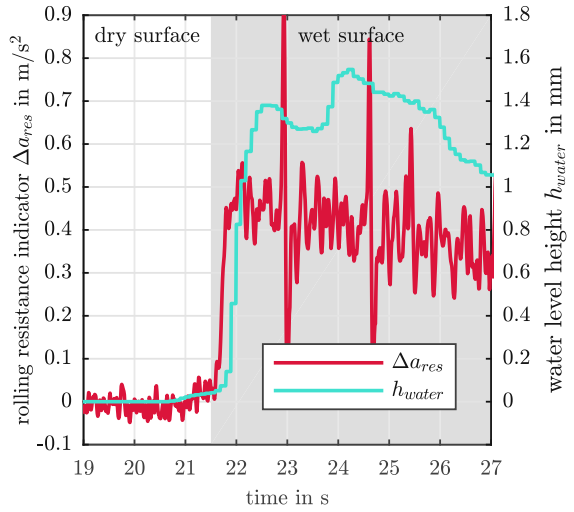

Figure 2.10.: Time plot of resistance measure during the change from dry to water-covered asphalt layer with ≈1.3 mm water level heights with (very) worn summer tires.

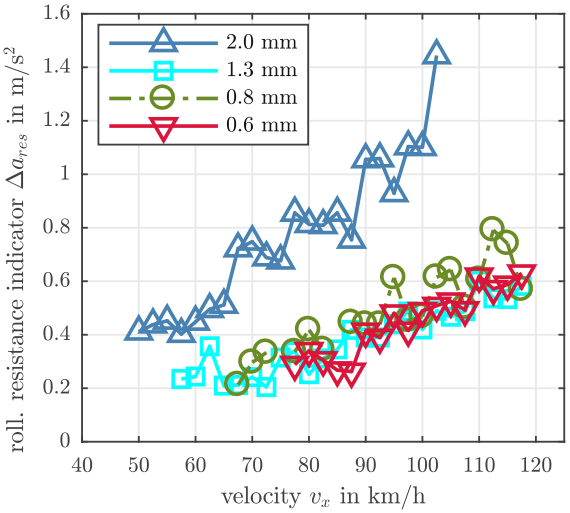

Figure 2.11.: Average values of resistance measure over speed for different water level heights with (very) worn summer tires and low tire pressure.

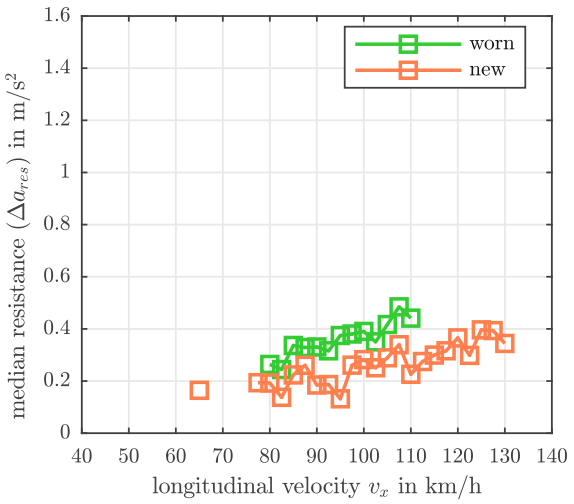

Figure 2.12.: Average values of resistance measure over speed for 1.1 mm water level height. Comparison of (very) worn and new summer tires with low inflation pressure for two different water level heights.

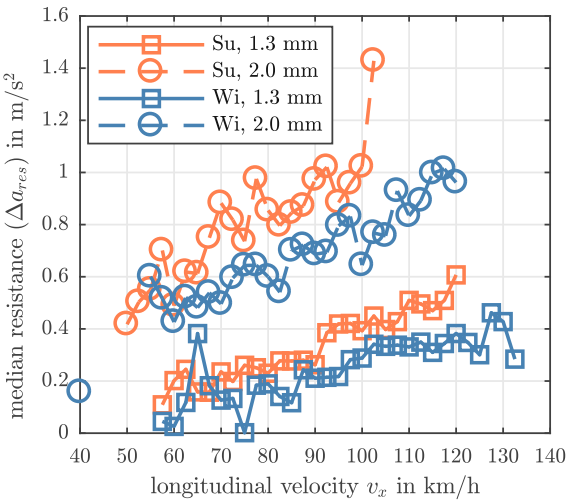

Figure 2.13.: Average values of resistance measure over speed. Comparison of (very) worn summer tires and new winter tires with low inflation pressure for two different water level heights.

pressure. Figure 2.15 shows that additional load and tire pressure lower the resistance change during partial aquaplaning.

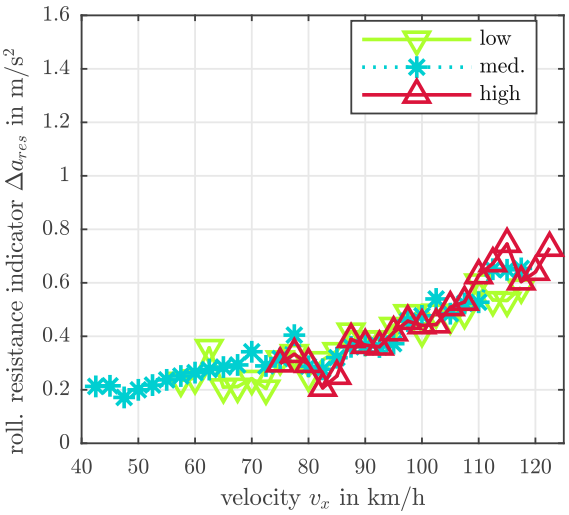

Figure 2.14.: Average values of resistance measure over speed for 1.3 mm water level height with (very) worn summer tires and varied inflation pressure.

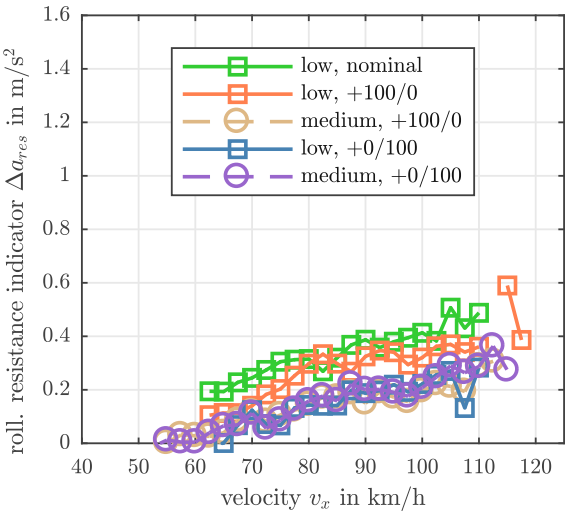

Figure 2.15.: Average values of resistance measure over speed for 1.2 mm water level height with (very) worn summer tires. Comparison of different pressures and additional loads of $\approx$ 270 kg on the front or rear axle.

Detection algorithm

The calculated acceleration difference Δa_x from Equation (2.9) is usually noisy and contains outliers because of disturbances, e.g. road irregularities, gear shifts, and noise in the input signals, Figure 2.10. Therefore a direct evaluation of the acceleration difference is not possible. Instead, a cumulative sum of the acceleration difference is used for evaluation, similar to the CUSUM change detector from [15].

2.3. Slip slope decrease

As shown theoretically in Equation (2.2) and Figure 2.2 bottom, a reduced tire contact patch length under partial aquaplaning conditions causes an early and significant decrease of the slip slope. This allows partial aquaplaning detection at typical driving maneuvers (constant velocity and moderate acceleration) without high utilization of maximum tire forces. Figure 2.16 shows slip curves from a (very) worn rear-driven tire, which were measured during a maneuver with moderate acceleration on dry asphalt and almost constant speed ($\approx$100 km/h) on a watered lane with 0.8 mm water level height. The total aquaplaning speed for this water depth and tire combination was approximately 20 km/h higher. Figure 2.17 to 2.20 show the average slip slope values

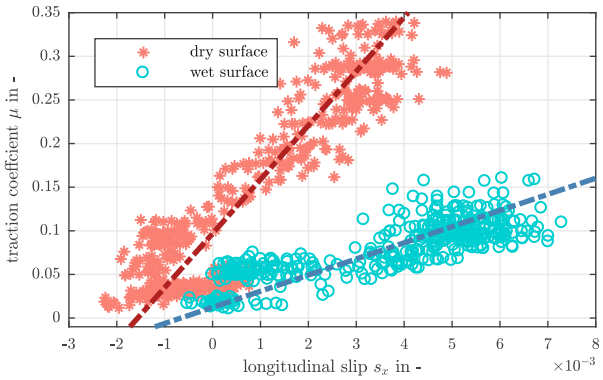

Figure 2.16.: Measured tire characteristics of a (very) worn rear tire on dry and water covered road with a water level height of 0.8 mm.

of the rear wheels of an RWD vehicle over velocity for several parameter variations (water height, tire pressure, tire type, load). Measured data points were categorized by longitudinal vehicle speed into bins and the slip slopes were determined with linear regression.

The slip slope curves for worn summer tires in Figure 2.17 give no clear indication of an influence of water level height on rear wheel slip slope decrease at one tire. A possible explanation is that the rear tires encounter a disturbed water surface since they are running in the tracks of the front wheels. The remaining amount of water in this track may be not directly dependent on the actual undisturbed water level height, as long the front tires do not experience total aquaplaning. Nevertheless, all curves decrease with increasing velocity like analytically predicted in Equation (2.2). Left wheel slip slopes are slightly higher and more nonuniform than those for the right tire. The reason for this difference may be explained by irregularities in the water level height, that were present on the left side of the lane due to the proximity to the sprinklers. Figure 2.18 shows the variation of tire pressures in three steps for the same tires as before and a constant water level height of 1.3 mm. The low and medium pressure curves are similar for both pressures, except for low velocities where only a few data points were available. The high-pressure curves show a significantly smaller slip slope for velocities far below aquaplaning speed. However, the decrease of slip slope is also much lower and the curves approach those for low and middle pressure at higher velocities, which might make early aquaplaning detection more difficult.

A comparison of slip slopes between worn summer tires and new winter tires on the rear axle in Figure 2.19 reveals that within the tested velocity ranges and water level height, winter tires do not experience any decrease in slip slope. Different axle loads and tire pressures are compared in Figure 2.20 for the rear tires. These result curves show only

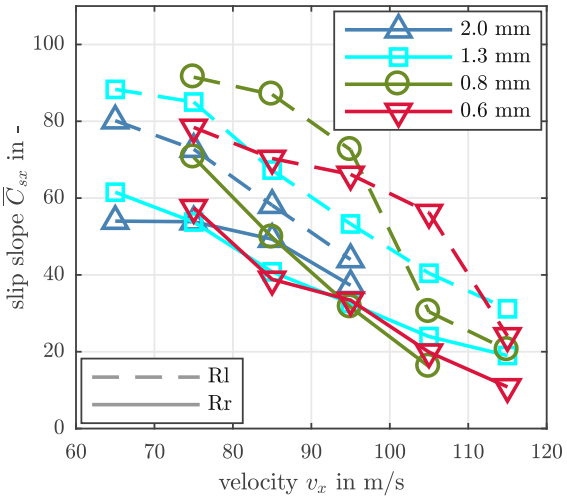

Figure 2.17.: Average slip slope values over velocity on driven rear tires with low tire inflation pressure and a variation of water level height.

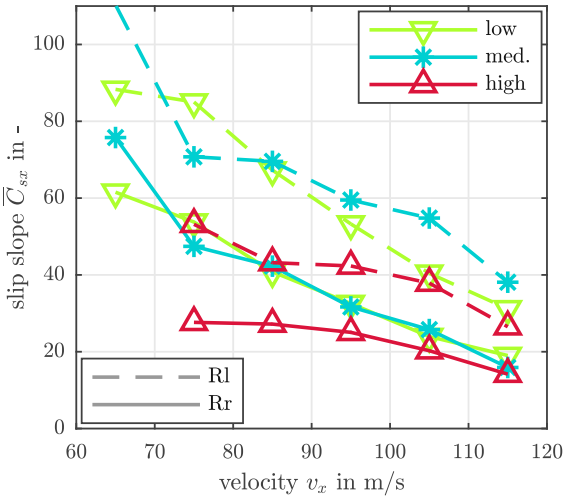

Figure 2.18.: Average slip slope values over velocity on driven rear tires with variation of tire inflation pressure and a water level height of 1.2 mm.

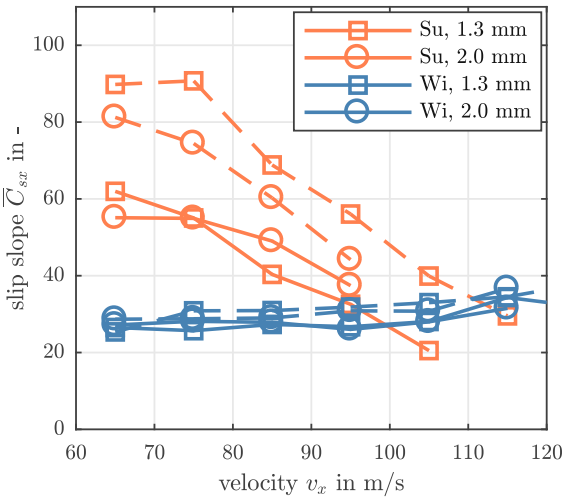

Figure 2.19.: Average slip slope values over velocity on driven rear winter and summer tires with water level heights of 1.3 and 2.0 mm.

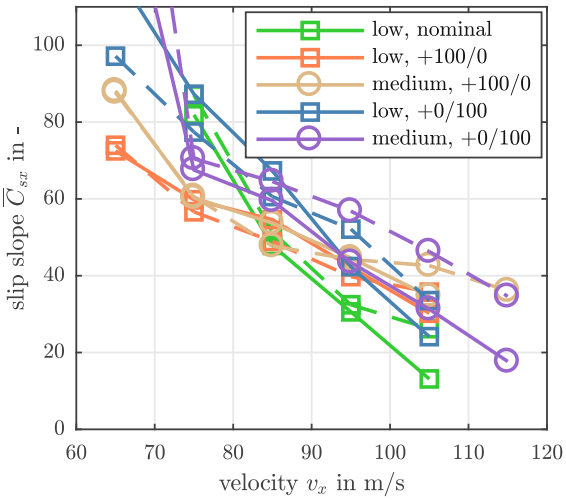

Figure 2.20.: Average slip slope values over velocity on driven rear tires with a water level height of 1.2 mm, low and medium tire inflation pressure and an additional load of 270 kg placed either at the front or rear axle.

a slight change of slip slope decrease with the different tire pressures and loads, but indicate that with additional load and tire pressure slip slope curves slightly increase.

Detection algorithm

For detection of the slip slope drop during partial aquaplaning estimator based approaches are used. If longitudinal velocity is available in sufficient quality, e.g. from non-driven wheels, a direct approach for slip slope estimation is suggested, [15]. For vehicles with all-wheel drive direct determination of longitudinal velocity from wheel speeds is not possible. In this case, an alternative strategy for slip slope estimation is presented in Chapter 3 based on differential slip and traction coefficient measures without longitudinal velocity. Independent of the specific slip slope estimation algorithm, the resulting slip slope estimate has to be continuously evaluated for the detection of partial aquaplaning. Since absolute slip slopes vary with tire type, load, pressure, etc. aquaplaning detection needs to compare the current slip slope drop relative to the nominal values on dry asphalt with the current tire and vehicle parameters. Therefore the maximum slip slope estimates within finite time periods are saved in a history for the current vehicle configuration (tire pressure, load, etc.). The continuous estimates are compared against the maximum of this history and allow for a determination of the relative decrease. Since slip slope drops can also occur on other low friction surfaces like ice, snow, and gravel, this information alone cannot identify partial aquaplaning unambiguous. In contrast to these surfaces, aquaplaning-induced slip slope drop is velocity dependent, a sufficient variation is not achieved during normal driving and may take too long for early detection. Additional information from other algorithms or sensors about the road condition is necessary to definitely identify aquaplaning.

2.4. Tie-Rod force change

The altered tire forces during (partial) aquaplaning in the contact patch influence the reaction forces of the tire, which is felt by the driver or can be measured in the steering or the tie rods. Therefore, analogue to the resistance calculation, aquaplaning can be detected by comparing nominal and measured steering/tie rod forces. The exact calculation of the tie rod forces is however difficult. It depends on steering and axle design and is very sensitive to parameter changes and disturbances. Especially slight changes in tire forces and aligning torques during partial aquaplaning may be too small for reliable evaluation. Measurement and calculation can substantially differ from each other if velocity is close or above the aquaplaning speed and already minor spin-ups/downs occur. In this case, even a very coarse tie rod force model allows reliable detection. The lateral tire forces are calculated using a two-wheel model and divided

onto the left and right wheels proportional to the quasi-static vertical loads. Tie rod forces are calculated from the tire forces with polynomial force transfer function based on MBD-simulations of the front axle.

Figure 2.21 shows a straight driving maneuver with slight deceleration and aquaplaning on the front right wheel of an AWD car. At the top, the velocity and wheel speeds of the front axle are plotted. In the second and third plots, the calculated and measured tie rod forces of the left and the right wheels are shown. There was (almost) no torque distributed to the front wheels so the wheel showed a series of spin-downs. Even very short spin-downs cause the measured tie rod forces to increase and differ from the calculated values on the right wheel, while calculated and measured forces on the left wheel without aquaplaning match well.

During a straight driving maneuver with two accelerations, Figure 2.22, torque is distributed to the front axle and spin-ups as well as spin-downs occur at both tires. At 18 s the front left tire has a slight spin-down that changes into a very short and small spin-up at 19 s, between 21 s and 22 s another small spin-down occurs and from 23 s to 24.5 s a strong spin-up. Both, spin-ups and spin-downs, cause an increase in the measured tie rod forces and differ significantly from the measured values.

A maneuver with almost constant velocity and sinusoidal steering is presented in Figure 2.23. The additional plot at the top of this figure shows the steering angle and lateral acceleration. The maximum later acceleration is up to 2 m/s^2 and the period of one cycle of steering is approximately 4 s. The wheel speed signals show a series of light spin-downs during this maneuver on both tires. The calculated and measured tie rod forces match well during steering, except when aquaplaning occurs. At 23 s both wheels have very short spin-downs and the comparison shows that measured tie rod forces differ from calculation, especially on the right side. From 26 s on a series of small spin-downs on the left wheel occur which also causes slight deviations in the tie rod force. Shortly after 27 s the right wheel also spins down concurrently with the left wheel, causing a loss of controllability of the vehicle and a decrease in lateral acceleration. Both tie rod force measurements increase significantly again.

2.5. Joint detection algorithm

The presented detection methods in the previous sections are based on individual aquaplaning phenomena. Their occurrence and detectability are dependent on different

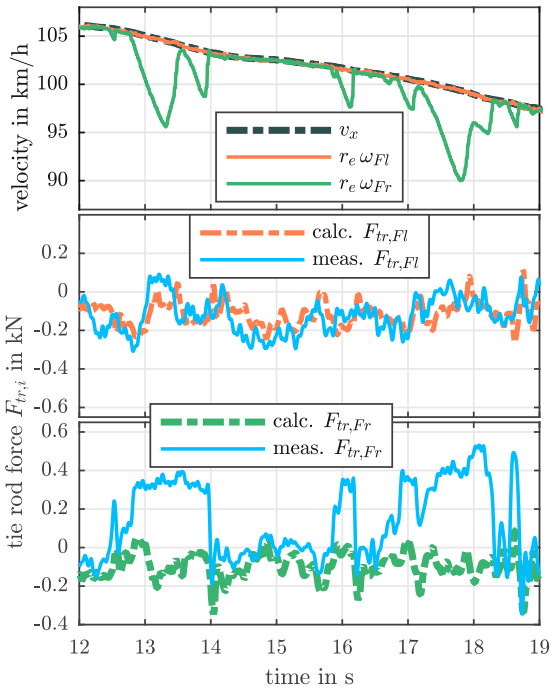

Figure 2.21.: Comparison of calculated and measured tie rod forces with full aquaplaning on non-driven front wheels during a straight driving maneuver with almost constant velocity.

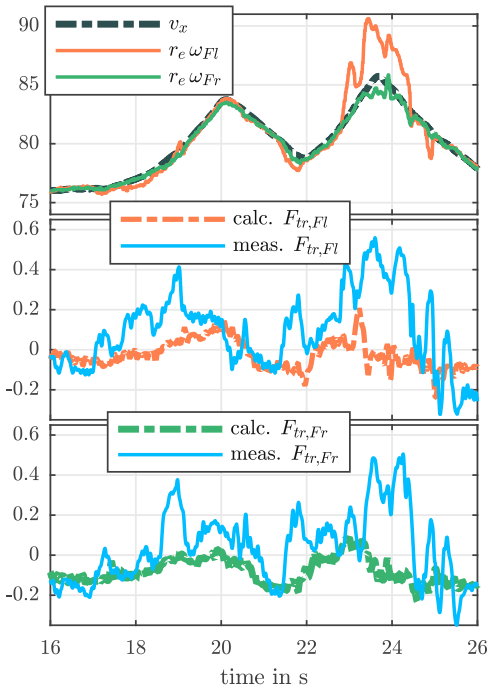

Figure 2.22.: Comparison of calculated and measured tie rod forces with partial and full aquaplaning on driven front wheels during a moderate acceleration straight driving maneuver.

parameters, e.g. vehicle velocity, drivetrain concept, tire type, age, and wear, etc. Many of these phenomena are also not unique to aquaplaning and additional information is necessary to reliably distinguish aquaplaning from other low-friction road surfaces. A combination of the single criteria allows the creation of a joint aquaplaning detection algorithm, with high sensitivity but also robustness against misdetections without the use of additional sensors. Two different implementations of a joint detection algorithm are presented here, the first based on key criteria and their combination detecting the individual phenomena and the second using the output of the individual methods from the previous sections.

Rolling resistance is a necessary criterion for (partial) aquaplaning detection, but since it depends on many tire and environmental parameters and is sensitive to disturbances, its use as a standalone detector for aquaplaning is limited. The first presented joint detection algorithm is used in two ways, first as an indicator for a critical water level height based on a cumulative sum, like in the previous single detection method above, and second as a necessary activation criterion for detection of other effects. All other criteria are evaluated in parallel and if at least one of them is fulfilled together with

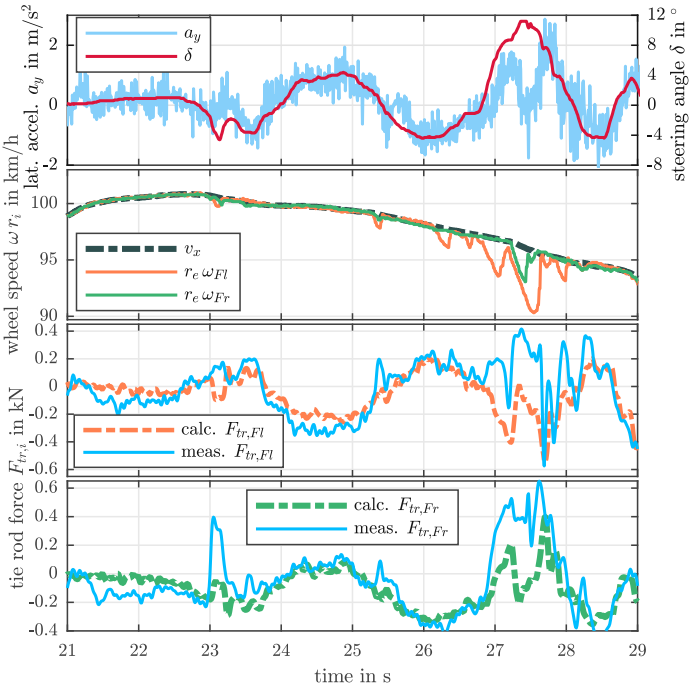

Figure 2.23.: Comparison of calculated and measured tie rod forces with full aquaplaning on non-driven front wheels during a slalom maneuver with almost constant velocity. Aquaplaning occurs on single wheels and on both wheels at the same time.

the rolling resistance criterion, an aquaplaning warning is generated, Figure 2.24. The following enumeration briefly describes these criteria:

- Excessive Wheel Spin-Down (1): If acceleration and velocity difference between wheel and vehicle exceeds certain (negative) thresholds, without negative tire forces, the wheels are considered to be in a spin-down and aquaplaning is detected.
- Minor Wheel Spin-Down (2): The absolute values and the difference of the variance of wheel acceleration difference are calculated on each vehicle side. If the absolute variance values on the non-driven wheels and the difference to the driven wheels exceed a certain value, the non-driven wheel speeds are lower than the vehicle speed and no negative forces are applied the minor wheel spin-down effect is detected.
- Wheel Spin-Up (3): Positive acceleration and speed differences between wheel and vehicle are detected as spin-ups. Additionally, these are distinguished between full and partial aquaplaning by the actual traction coefficient.
- Slip-Slope Drop (4): Slip slope is continuously estimated by an estimator, e.g. the method presented in Chapter 3, and its historic values are saved for comparison.

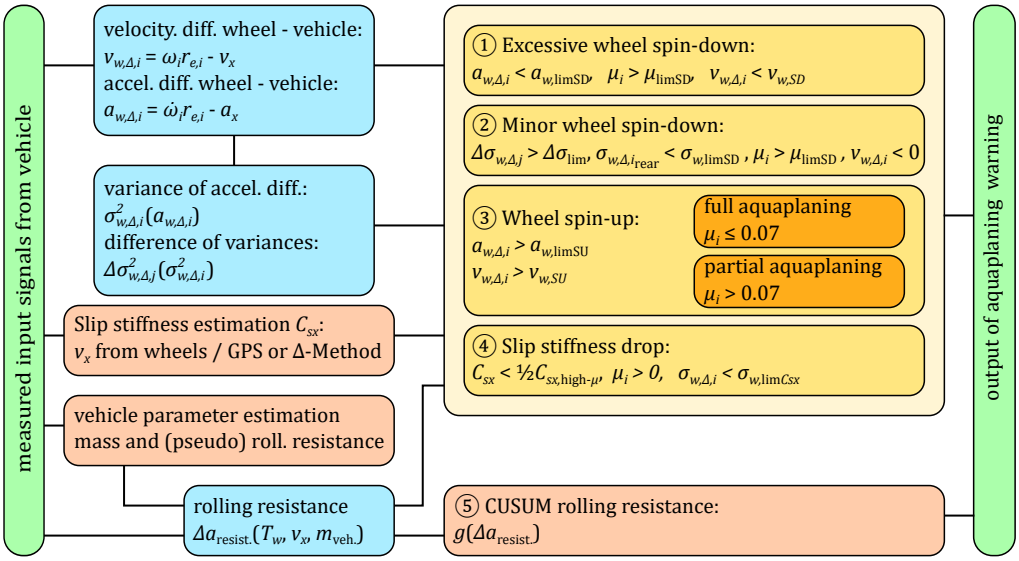

Figure 2.24.: Diagram of joint detection algorithm based on a combination of criteria for detection of typical aquaplaning phenomena.

Aquaplaning is detected if the actual slip slope decreases below half of the maximum historic value, tires are driven and the wheel acceleration variance is below a defined threshold.

- Resistance detection (5): The CUSUM-based single effect method is used as an additional indicator for a critical water level height.

All criteria for wheel spin-up and spin-down use mainly acceleration differences between wheel and vehicle for detection, which are readily calculated from onboard measurements of the ESC in high quality. Compared to methods based on absolute slip values, which need high-quality velocity signals, the speed and acceleration differences used for these criteria allow detection even with coarse velocity signals, e.g. from average overall wheel speeds, estimators, etc., since they are only used for the distinction between spin-up and spin-down. Slip slope detection however is more complex and has to be chosen depending on the drive-train concept and available measurement signals and quality. The longitudinal velocity-free method presented in Chapter 3 is a practical solution for slip slope estimation and detection of changes, especially for all-wheel drive vehicles.

For reliable detection of rolling resistance changes, the model parameters (vehicle mass, drag coefficient, nominal rolling resistance on dry surfaces) have to be known. To determine these, a separate module is proposed, as presented in [39] and [40], that

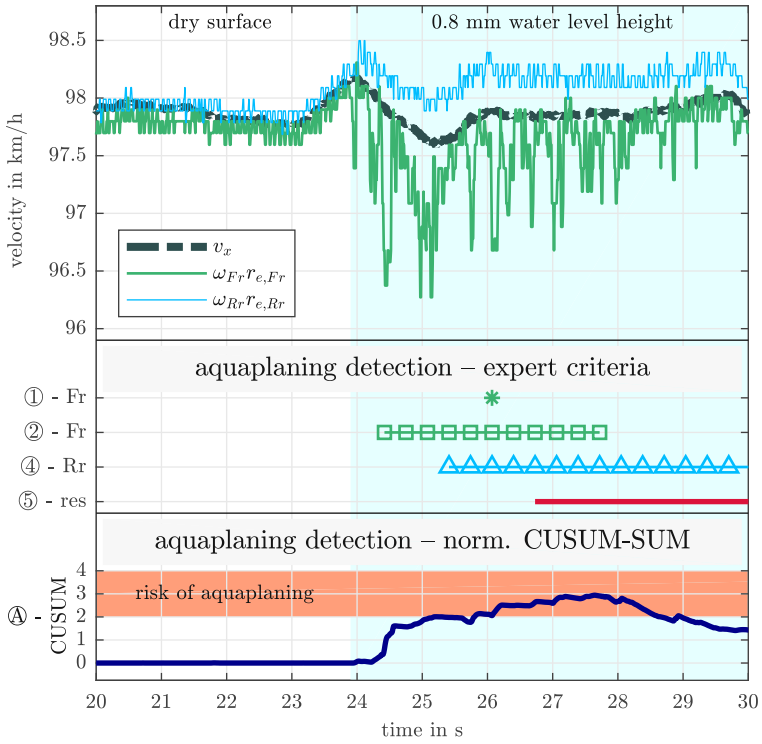

Figure 2.25.: Wheel speed signals at minor aquaplaning with detection bits of joint detection method based on expert criteria, middle plot, and CUSUM-based detection algorithm, bottom plot.

estimates the parameters during periods when aquaplaning is unlikely, e.g. low velocities, external information of dry road surface, etc.

The alternate joint detection algorithm uses a combination of signals from the standalone methods presented in the previous section for detection. For spin-ups, large spin-downs and rolling resistance the CUSUM values of the individual methods are scaled and for minor spin-downs, the variation measure is scaled and added to a total sum measure, Equation (2.11). In this equation, the slip slope drop is not considered yet. It can be added using a measure of the slip slope reduction relative to the dry slip slope values. This new CUSUM-sum is evaluated for aquaplaning detection with a threshold that is chosen to achieve the desired sensitivity. Additional scaling factors can be introduced at every term to adapt the behavior and sensitivity relatively between the individual effects.

$$g_{\text{gesamt},k} = \frac{g_{\text{SU},ax,k}}{g_{\text{SU,max}}} + \frac{g_{\text{SD},ax,k}}{g_{\text{SD},ax,\text{max}}} + \frac{g_{\text{SD},\sigma^2,k}}{g_{\text{SD},\sigma^2,\text{max}}} + \frac{\min(\Delta\sigma^2_{\omega,\Delta,j}, \Delta\sigma^2_{\omega,\text{max}}) - \Delta\sigma^2_{\omega,\text{min}}}{\Delta\sigma^2_{\omega,\text{max}} - \Delta\sigma^2_{\omega,\text{min}}} \quad (2.11)$$

Figure 2.25 shows a constant velocity maneuver below full aquaplaning speed on a watered lane with 0.8 mm water level height. After entering the water layer rear tire slip increases significantly, while at the same time, a series of minor spin-downs occur at the front right tire. The middle part of the figure shows the detection bits of the joint algorithms based on the expert criteria relevant for this maneuver. The minor spin-down criterion (2) detects the aquaplaning in less than 0.5 s after entering the watered lane at 24 s and keeps the detection bit active until 27.5 s when the magnitude of the minor spin-downs decreased to a very low level. The slip increase at the rear right tire is detected by the slip slope based criterion (4) after approximately 1.5 s. The slip slope drop detection lasts until the end of the plotted time interval, as the rear tire is continuously driven and the slip remains high. At 26 s even a detection of large spin-downs by criterion (1) is visible. The resistance-based detection criterion (5) of a critical water layer, based on the single effect method from Section 2.2, is parameterized for robust detection and detects aquaplaning conditions at 2.5 s after entering the water layer. The bottom plot shows the CUSUM-sum signal calculated from the individual methods and the threshold for aquaplaning detection. The CUSUM-sum signal increases after 0.5 seconds after entering the watered lane but does not reach the detection threshold. At 25 s it slightly crosses the threshold indicating aquaplaning but decreases again. From 25.8 s until 28.8 s it stays active again.

Chapter 3

Slip slope estimation and change detection

3.1. Tire characteristics in the micro-slip region

As a viable measure for changes in friction potential several papers [12] [13] [14] [15] suggested changes in the initial slip slope of the tire characteristics. A derivation of the slip slope based on the brush tire model is given in [11] starting with the definition for longitudinal tire forces at small slips:

$$C_{s_x} = \frac{\partial F_x}{\partial s_x}|_{s_x=0} = \frac{\partial}{\partial s_x}\left(2c_{px}a^2 s_x\right) = 2c_{px}a^2 \tag{3.12}$$

with the tire contact patch length a, bristle stiffness c_{px}, and the longitudinal slip $s_{x,i}$ defined as:

$$s_{x,i} = \frac{\omega_i r_{e,i} - v_x}{\omega_i r_{e,i}} \tag{3.13}$$

This formulation based on a simple physical model of the tire behavior does not explain any explicit relation with the friction coefficient, the slip stiffness is a pure tire parameter dependent on e.g. material, design, wear, etc. Similar derivations of the slip stiffness, based on the brush tire model and the LuGre model, are also given in [13]. However, in the presence of an additional layer, e.g. gravel, snow, etc., the slip slope decreases significantly. A possible explanation for this phenomenon can be compliance of the intermediate layer [5] [13] [14], which acts like an additional ground stiffness in series with the bristle stiffness. Figure 3.1 shows measured tire curves from a production car for the same tire on different surfaces, which clearly allow a distinction between the surfaces. The maximum traction coefficients for snow on asphalt and snow on ice

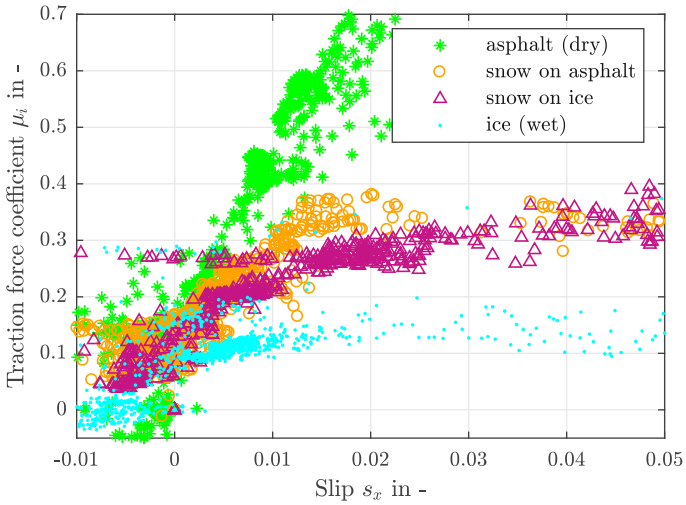

Figure 3.1.: Measured tire characteristics of a rear tire of an AWD vehicle on different surfaces (dry asphalt, snow on asphalt and on ice, wet ice)

are almost the same within the plotted slip range, but the initial slip slope and the transition zone between the linear region and saturation are different.

Slip curves on dry ice or wet surfaces without a continuous water layer do not show any significant changes in their linear region, [13], or may have even slightly higher slopes [15] [24]. Therefore, a drop in the initial slip slope is a good indicator of decreased friction potential even though it does not necessarily happen and it is not possible to give a direct analytic relation between these two tire parameters.

On wet surfaces with a continuous water layer, the slip slope also decreases depending on tire parameters, water height, and longitudinal vehicle velocity. The phenomenon behind this slip slope change is different than on solid surfaces and is a result of reduced tire contact patch length in contact with the solid surface. Measurement results, a detailed explanation of the phenomenon, and analytic relations between contact length and slip stiffness as well as maximum traction coefficient are given in Chapter 2.

3.2. Slip slope detection method

For the determination and estimation of longitudinal tire characteristics, slip and traction/braking force coefficient have to be determined. The slip definition, Equation (3.13), requires the current longitudinal velocity v_x of the tire, its wheel speed ω, and the effective rolling radius r_e. Wheel speed ω is measured directly by the wheel speed sensor and available in sufficient quality. Effective tire radii have to be determined

corresponding to the longitudinal reference velocity v_x during maneuvers without longitudinal forces from traction or braking at the tire. Depending on the requirements and available sensors, the reference velocity source has to be chosen and any time delays have to be taken into account, e.g. from GPS. If the reference velocity v_x is directly determined from other wheel speed signals, no additional time delay or errors from different signal processing transfer functions occur, but the slip calculation is limited to maneuvers during free rolling of the reference tires. Especially for all-wheel drive cars such situations may occur rarely, making absolute slip calculation difficult without additional velocity signal sources. The traction force coefficient relies on an accurate estimate/measurement of the longitudinal and vertical tire forces. To allow slip slope estimation without explicit longitudinal velocity information an approach based solely on wheel speed and torque measures from both axles is suggested. The basis of the algorithm is the linear tire model for slip slope estimation from [15]:

$$\mu_i = \overline{C}_{s_x,i} \, (s_{x,i} + \delta_{s_x,i}) \quad \text{with} \quad i = F, R \tag{3.14}$$

that relies on two parameters: the slip slope parameter C_{s_x} and a slip-offset δ_{s_x}. The slip definition from Equation (3.13) for the front and rear axle is used to eliminate the longitudinal velocity by substituting both slip definitions into each other resulting in e.g. the following equation for the front slip $s_{x,F}$:

$$s_{x,F} = \underbrace{\frac{r_{e,F}\,\omega_F - r_{e,R}\,\omega_R}{r_{e,F}\,\omega_F}}_{s_{x,\Delta,F}} + \frac{r_{e,R}\,\omega_R}{r_{e,F}\,\omega_F}\, s_{x,R} \tag{3.15}$$

The first fraction term $s_{x,\Delta,F}$ is the relative velocity difference between the front and rear axle wheel speeds and therefore called differential slip (formulated at the front axle). Rearranging of the equation above shows that it can be formulated as a scaled difference between the axle slips:

$$s_{x,\Delta,F} = \frac{r_{e,F}\,\omega_F - r_{e,R}\,\omega_R}{r_{e,F}\,\omega_F} = s_{x,F} - \frac{r_{e,R}\,\omega_R}{r_{e,F}\,\omega_F}\, s_{x,R} \tag{3.16}$$

Generally, the slip slope on the front and rear axle will differ because of tire type, wear, pressure, load, etc and it will be necessary to account for both in a longitudinal velocity-free slip slope estimation. These can change quickly on different road surfaces, but it can be assumed that this change is proportional on both axles. Instead of an individual estimation, a slip slope ratio λ of the (normalized) slip slope on the front and

rear axle is introduced in Equation (3.17) and estimated together with the slip slope of one axle. This additional parameter allows for the continuous adaption of slowly varying differences between front and rear axle stiffness while sudden drops of the slip slope on both axles can be detected quickly.

$$\lambda = \frac{C_{s_x,R}/F_{z,R}}{C_{sx,F}/F_{z,F}} = \frac{\overline{C}_{s_x,R}}{\overline{C}_{sx,F}} \quad \Rightarrow \quad \overline{C}_{s_x,R} = \lambda\, \overline{C}_{s_x,F} \tag{3.17}$$

With Equation (3.14) for both, the front and rear axle, the definition of the differential slip from Equation (3.16) and the slip slope ratio λ the following relation for slip slope estimation with differential measures, formulated at the front axle, is derived:

$$s_{x,\Delta,F} = \underbrace{\left(\mu_F - \frac{1}{\lambda}\frac{r_{e,R}\,\omega_R}{r_{e,F}\,\omega_F}\,\mu_R\right)}_{\mu_{\Delta,F}} \frac{1}{\overline{C}_{s_x,F}} + \underbrace{\left(\delta_F - \frac{r_{e,R}\,\omega_R}{r_{e,F}\,\omega_F}\delta_R\right)}_{\bar{\delta}_F} \tag{3.18}$$

The term within the first brackets is the scaled difference between the traction coefficients of the wheels of opposite axles scaled with the slip slope ratio λ, and is referred to as the differential traction coefficient $\mu_{\Delta,F}$. Equation (3.18) is formulated for the front axle differential slip, the analogue rear axle formulation reads:

$$s_{x,\Delta,R} = \underbrace{\left(\mu_R - \lambda\frac{r_{e,F}\,\omega_F}{r_{e,R}\,\omega_R}\,\mu_F\right)}_{\mu_{\Delta,R}} \frac{1}{\overline{C}_{s_x,R}} + \underbrace{\left(\delta_R - \frac{r_{e,F}\,\omega_F}{r_{e,R}\,\omega_R}\delta_F\right)}_{\bar{\delta}_R} \tag{3.19}$$

The full derivation of both equations is explained in Appendix A. Additionally the equations can be used with single wheel speeds and traction coefficients of opposite tires at one vehicle side enabling individual estimation of slip slope at both sides of the vehicle. In the case of just one driven axle the slip-free wheel speed of the opposite axle is equal to the absolute vehicle speed. Hence, Equations (3.18) and (3.19) allow the direct estimation of the true slip slope of the driven axle similar to algorithms based on equation (3.14) like in [15].

Parameter estimation

Because of the slip slope ratio λ in the differential traction force coefficient and the slip slope parameter $\overline{C}_{s_x,F}$, Equation (3.18) and (3.19) are nonlinear in their parameters.

The individual tire slip offset parameters are estimated together as a generalized offset parameter of the differential slip $\overline{\delta}_F$. For estimation of the slip slope parameter Equation (3.18) or (3.19) is implemented as an output equation of e.g. extended Kalman filters:

$$y_k = h_k(\underline{x}_k, v_k) = \left(\mu_{i,k} - \beta_i \frac{r_{e,j}\,\omega_{j,k}}{r_{e,i}\,\omega_{i,k}}\mu_{j,k}\right)\frac{1}{\overline{C}_{s_{x,i,k}}} + \overline{\delta}_{i,k} + v_k \qquad i = F, R,\ j = R, F, \tag{3.20}$$

$$\beta_F = \frac{1}{\lambda} \quad \text{and} \quad \beta_R = \lambda \tag{3.21}$$

Since the λ parameter is either in the denominator, Equation (3.18), or the numerator, Equation (3.19), depending on the formulation of the output equation w.r.t. the front or rear axle it was substituted with a new parameter β_i in Equation (3.20). The resulting parameter vector reads:

$$\underline{x}_k = \begin{bmatrix} \frac{1}{\overline{C}_{s_x\,i\,k}} \\ \beta_{i,k} \\ \overline{\delta}_{i\,k} \end{bmatrix} \qquad i = F, R,\ j = R, F, \tag{3.22}$$

The choice of the parameters as slowly changing (slip stiffness ratio and (differential) slip offset) and fast-changing (slip slope) allows for a robust and sensitive parameterization of the estimator. An additional change detection algorithm based on the CUSUM [15], improves estimation behavior further. The positive and negative prediction error $\epsilon = y_k - h_k(\underline{x}_k, 0)$ is accumulated in the standard CUSUM algorithm and compared against a threshold to detect a change in the parameters:

$$\nu_{k,cusum} = \epsilon_k \tag{3.23}$$

$$\underline{g}_k = \underline{g}_{k-1} + \begin{bmatrix} \nu_{k,cusum} \\ -\nu_{k,cusum} \end{bmatrix} - \underline{\zeta} \tag{3.24}$$

Since the prediction error can take positive as well as negative values for the same parameter change, depending on the sign of the differential slip, an adapted measure for the CUSUM is proposed. The prediction error ϵ is multiplied by the sign of the differential slip $s_{x,\Delta,k}$:

$$\nu_{k,cusum} = \mathrm{sgn}(s_{x,\Delta,k})\,\epsilon_k \tag{3.25}$$

A graphical interpretation of these two versions of CUSUM input is presented in Figure 3.2a and the resulting effect on the CUSUM values in Figure 3.2b.

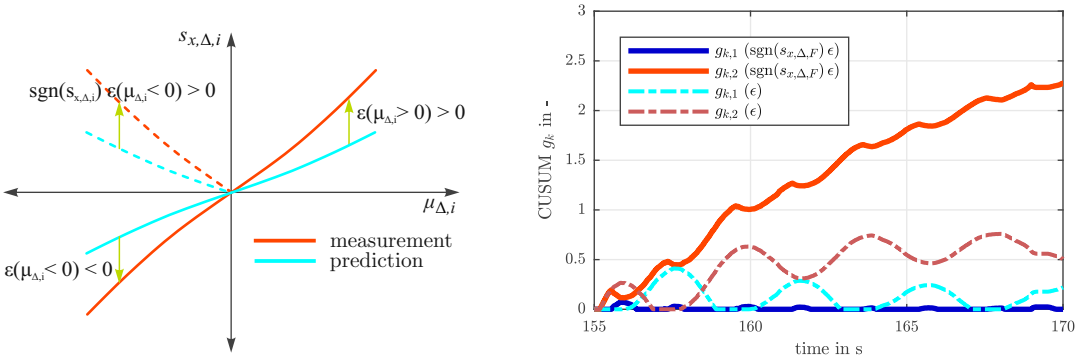

(a) (b)

Figure 3.2.: (a) Calculation of $\nu_{k,cusum}$ from prediction error ϵ_k and differential slip $s_{x,\Delta,k}$, and (b) time history of g_k applying (3.23) and (3.25)

For use of the method with measurement signals additional activation criteria, e.g. minimum/maximum differential slip/traction coefficient criteria values, minimum velocity, maximum acceleration, etc, were implemented for the estimator.

Sensitivity

A graphical interpretation of scaling and calculation of differential slip and traction coefficient for the slip slope equation formulated at the front axle is depicted in Figure 3.3. The original slip curve of the rear axle, left plot, is scaled along the traction coefficient and slip axis using the slip slope ratio and the ratio of the actual wheel speeds at the front and rear axle. The resulting curve is shown together with the front slip curve in the right plot of Figure 3.3. The slip slope (of the front tire) can now be determined directly from the differential slip and traction coefficient, as long the (transformed) slips on both axles are not equal.

In Figure 3.4a the whole range of possible differential traction coefficients close to zero slip and differential slip formulated at the front axle is plotted as surfaces for two different maximum traction coefficients ($\mu = 1.0$ and 0.4) in the "slip"-"differential slip"-"differential traction coefficient" space ($s_{x,F}$-$s_{x,\Delta,F}$-$\mu_{\Delta,F}$). These surfaces were generated using a Brush tire model with different nominal axle loads ($F_{z,F}/F_{z,R} = 40/60$). Slip

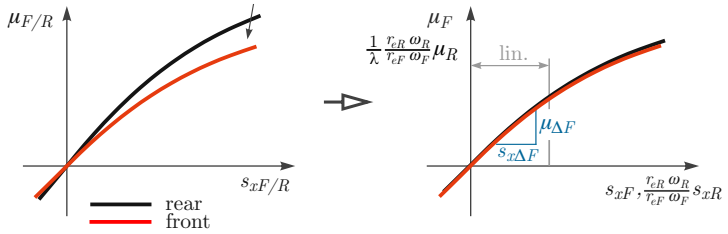

Figure 3.3.: Scaling of the slip-curves and calculation of differential slip and differential traction coefficient

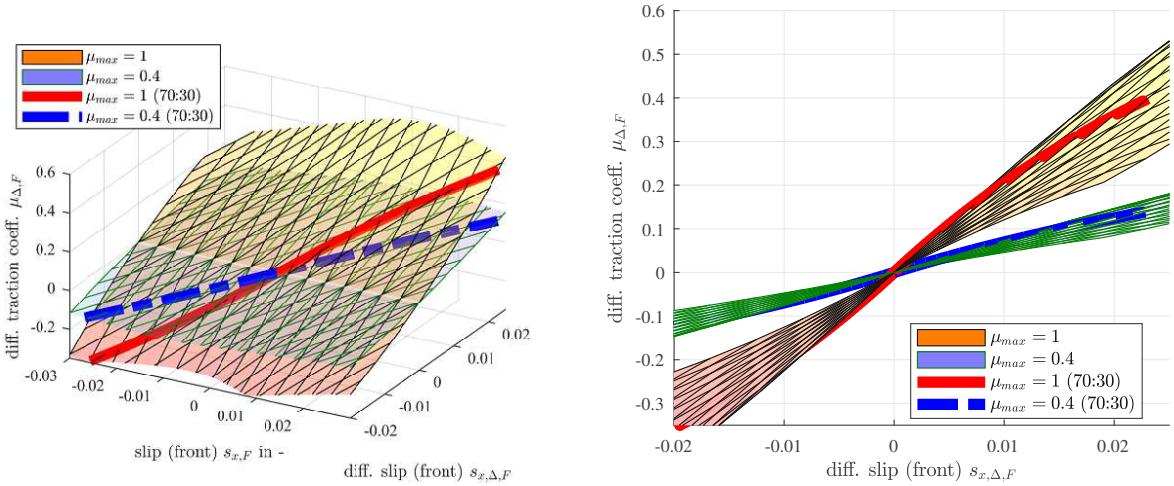

(a) Differential traction coefficient trajectories for a fixed torque distribution ($\nu = 0.3$) in the $s_{x,F}$-$s_{x,\Delta,F}$-$\mu_{\Delta,F}$-space

(b) Projection of surface and differential traction coefficient trajectories onto the $s_{x,\Delta,F}$-$\mu_{\Delta,F}$ plane.

Figure 3.4.: Surface of differential traction coefficient over front axle slip $s_{x,F}$ and front axle differential slip $s_{x,\Delta,F}$ for high (dry surface) and low (snowy surface) nominal maximum traction force coefficients and slip slopes

stiffness values on the front and rear axle tires were reduced equally by two-thirds for the low friction coefficient surface. Assuming fixed torque distributions the possible differential traction coefficients are lines along these surfaces (high $\mu_{\max}$: red solid and low $\mu_{\max}$: blue dotted). In case there is no absolute longitudinal velocity and from the method Equation (3.18) the absolute slip is not known and these surfaces and lines can only be determined as their projections onto the $s_{x,\Delta,F}$-$\mu_{\Delta,F}$ plane, Figure 3.4b. For the given initial slip slopes, maximum traction coefficients, and torque distribution the red and blue lines can be distinguished clearly. An estimator based on Equation (3.18) (or the equivalent rear axle formulation), detects the initial (differential slip) slope of the projected lines and allows reliable distinction between the surfaces for the given torque distribution.

Different fixed torque distributions alter the orientation and form of the lines on the

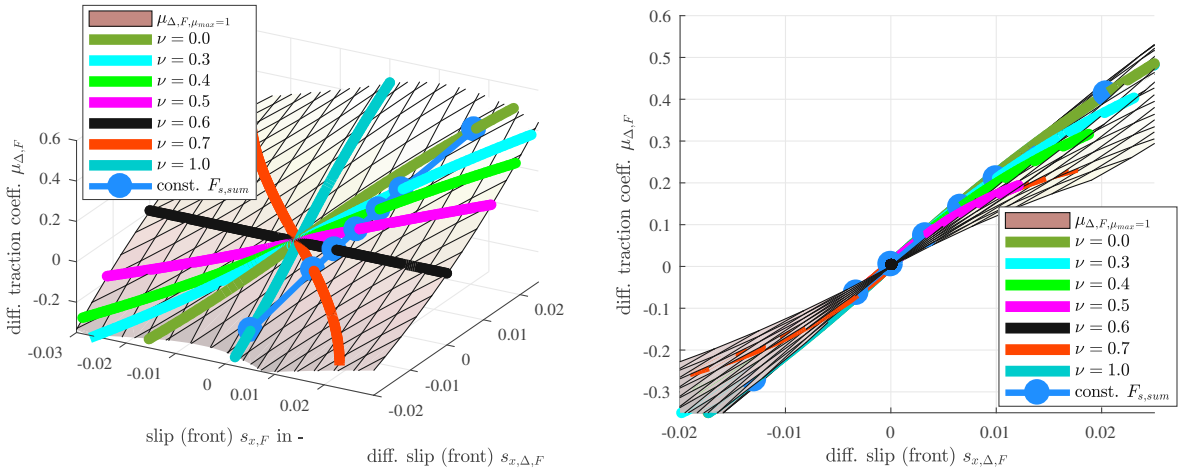

(a) Colored lines show differential traction force coefficient paths for varying fixed torque distribution from pure front- to pure rear-wheel drive.

(b) Projection of surface and varied fixed torque ratio paths of differential traction coefficient onto the differential slip/traction coefficient surface.

Figure 3.5.: Surface of differential traction coefficient over front axle slip $s_{x,F}$ and front axle differential slip $s_{x,\Delta,F}$ with variation of fixed torque distributions ν and variation of torque distribution for a fixed sum of longitudinal forces $F_{x,\mathbf{sum}}$.

differential traction coefficient surface. In Figure 3.5a differential traction coefficient trajectories for a variation of fixed torque distributions are plotted on the high-friction surface from pure front-wheel drive ($\nu = 0$) to pure rear-wheel drive ($\nu = 1$). The torque distribution mainly influences the orientation of these trajectories on the surfaces. For fixed torque distribution ratios, all lines cross the origin at zero (differential) slip and differential traction coefficient but are clearly distinguishable on the three-dimensional surface. In pure front-wheel drive configuration the differential slip $s_{x,\Delta,F}$ is equal to the absolute slip on the front axle $s_{x,F}$, resulting in a diagonal trajectory, Figure 3.5a solid dark green line. Pure rear-wheel drive ($\nu = 1.0$) results in a straight trajectory above the $s_{x,F} = 0$ axis. The dark blue line with circle markers shows a variation of the torque distribution for a fixed longitudinal acceleration ($F_{x,\text{sum}}$ =const.) from pure front to pure rear wheel drive. In the projection on the differential slip/traction coefficient plane, Figure 3.5b, differential traction coefficient paths with a distribution close to $\nu = 0.6$ are oriented towards the $s_{x,\Delta,F}$-$\mu_{\Delta,F}$ plane and an initial (differential) slip slope cannot be reliably detected. In such situations, the slip on both axles is similar regardless of its absolute values. This results in differential slip and traction coefficients always being close to zero. Hence, these situations need to be avoided to achieve high availability and quality of the differential slip slope estimation.

3.3. Active excitation

Long periods of constant velocity or slow acceleration lead to almost constant traction coefficients and slip values on the tires. This causes an aggregation of measurement data points in a narrow area of the μ-s_x and $s_{\Delta,x}$-μ_Δ plane and makes an estimation of a slope impossible. Also in the previously described case of equal slip on both axes (e.g. $\nu = 0.6$ in the presented Figures 3.5) (differential) slip slope estimation is not possible. Data points are then grouped around the origin of the $s_{\Delta,x}$-μ_Δ plane independent of absolute actual slip and traction coefficient values. Since the former situations occur frequently in everyday operations and the latter ones may be requested by stability control for safe operation in critical conditions, the availability of estimated signals can be low.

The proposed solution for increasing availability and sensitivity is an active excitation of the individual longitudinal tire forces on the front and rear axle $F_{x,F}$ and $F_{x,R}$, while keeping their sum constant as required to maintain the currently requested velocity/acceleration from the driver or robot. The total axle forces are the sum of the nominal forces $F_{x,0,F}$, $F_{x,0,R}$ requested by the drive torque distribution algorithm and the additional excitation forces $F_{x,\mathrm{exc}}(t)$ with opposite signs for front and rear axle:

$$F_{x,F} = F_{x,0,F} + F_{x,\mathrm{exc}}(t) = (1-\nu)\, F_{x,\mathrm{sum},0} + F_{x,\mathrm{exc}}(t) \tag{3.26}$$

$$F_{x,R} = F_{x,0,R} - F_{x,\mathrm{exc}}(t) = \nu\, F_{x,\mathrm{sum},0} - F_{x,\mathrm{exc}}(t) \tag{3.27}$$

Simulation model

For the evaluation of the presented slip slope estimator with active force excitation a half car model, equation (3.28) to (3.32), with a Brush tire model was used to generate input data. Since only constant velocities or low levels of acceleration and therefore traction coefficient utilization as well as slow changes of these are assumed, transient tire and vehicle body behavior was considered negligible. These types of maneuvers were simulated for different high- and low-friction surfaces with corresponding tire parameters.

$$\dot{x}_1 = \frac{1}{m}\left(F_{x,F} + F_{x,R} - C_D\, x_1^2\right) \tag{3.28}$$

$$\dot{x}_2 = \frac{1}{I_F}\left(M_F(t) - r_{l,F} F_{x,F} - r_{D,F} F_{z,F}\right) \tag{3.29}$$

$$\dot{x}_3 = \frac{1}{I_R}\left(M_R(t) - r_{l,R} F_{x,R} - r_{D,R} F_{z,R}\right) \tag{3.30}$$

$$F_{z,F} = F_{z,F0} - \Delta F_z(\dot{x}_1) \tag{3.31}$$

$$F_{z,R} = F_{z,R0} + \Delta F_z(\dot{x}_1) \tag{3.32}$$

with the vehicle mass m, wheel inertia for the whole axles $I_{F/R}$, drag coefficient $C_D = 0.5\, A\, c_d\, \rho$, the loaded wheel radii $r_{l,F/R}$, the rolling resistance coefficient $r_{D,F/R}$ and the quasi-static load transfer:

$$\Delta F_z = \frac{m\, h}{l_F + l_R}\, \dot{x}_1 \tag{3.33}$$

with the distance from the center of mass to the front and rear axle $l_{F/R}$ and its height over ground h. The nominal, normalized slip slope on both axles on the high friction surface is 30, which is reduced to 10 on the low friction surface.

Type and parameters of excitation force

The excitation force $F_{x,exc}(t)$ can be a periodic, transient, or random function within the limits of possible drive-train and tire dynamics. However, for drive comfort and safety the change rates and amplitudes should be small enough that passengers do not feel the variation and that critical utilization of the friction potential is avoided, e.g. ($\mu_i \leq 0.2$). The following functions (3.34)-(3.37) are examples of active excitation signals that are suitable for persistent tire force excitation. In (3.34) and in Figure 3.8a, top left, a triangular function is presented. The amplitude A_{exc} can be chosen as an absolute force, traction coefficient, or relative to the nominal longitudinal tire forces.

$$F_{x,\text{exc}}(t) = A_{\text{exc}}\, f_{\text{tri}}(t) \tag{3.34}$$

with

$$f_{\text{tri}}(t) = (2 \cdot \left(1 - (\frac{2}{\tau}t - \frac{1}{2}) \bmod 2\right) \cdot \text{sign}\left(1 - (\frac{2}{\tau}t - \frac{1}{2}) \bmod 2\right) - 1) \tag{3.35}$$

A sinusoidal function is another suitable excitation waveform, Figure 3.8b top left, with the same amplitude A_{exc} and period τ:

$$F_{x,\text{exc}}(t) = A_{\text{exc}} \sin\left(\frac{2\,\pi}{\tau}\,t\right) \tag{3.36}$$

A third example of an excitation function is a combination of periodic ramps and constant levels, Equation (3.37) and Figure 3.8c is presented. The parameters of the exemplary periodic ramp function where chosen so that the ramp and constant value sections have a length of $\tau/6$:

$$F_{x,\text{exc}}(t) = A_{\text{exc}} \min\left(\max\left(1.5 \cdot f_{\text{tri}}(t), -1\right), 1\right) \tag{3.37}$$

As a reference for maximum periodic excitation levels an alternating step excitation waveform is chosen, Figure 3.8d:

$$F_{x,\text{exc}}(t) = A_{\text{exc}} \cdot \text{sign}\left((\frac{2}{\tau}t) \bmod 2 - 1\right) \tag{3.38}$$

To assess the influence of the excitation on the estimator performance different excitation function types, time constants and amplitudes are used to compare the resulting slip slope estimates. The noise-free input signals for these estimation results were generated with the vehicle model from Section 3.3. In general, estimator and change detection parameterization and activation criteria have a major influence on the behavior of the slip slope estimation and are briefly addressed at the end of this section. In Figure 3.6 and 3.7 estimated slip slopes for triangular, sinusoidal, periodic/transient ramps and steps are compared for a constant velocity and an acceleration of $a_x \approx 1$ m/s^2. Periodic step excitation leads to the fastest detection of a slip slope drop after approximately 1 s. The other excitation functions cause the estimator to detect the slip slope drop at above 2 s with the periodic ramp excitation being slightly faster. The influence of the minimum differential traction force coefficient criteria, which is necessary for practical use with measurement data, can be seen in Figure 3.7 which shows periods without active excitation (light-colored thin lines).

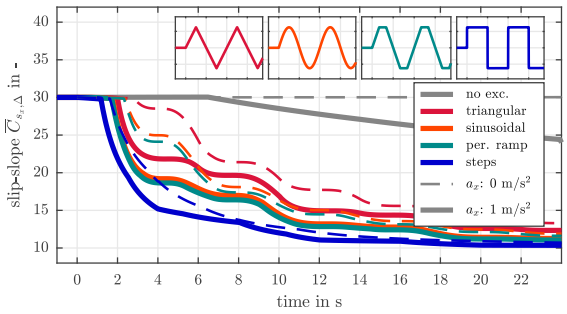

Figure 3.6.: Comparison of estimated slip slope time histories for different excitation functions from simulated signals: $A_{\text{exc}} = 250$ N, $a_x = 1$ m/s^2, $\tau = 8$ s. The minimum differential traction force coefficient criteria were deactivated for this plot.

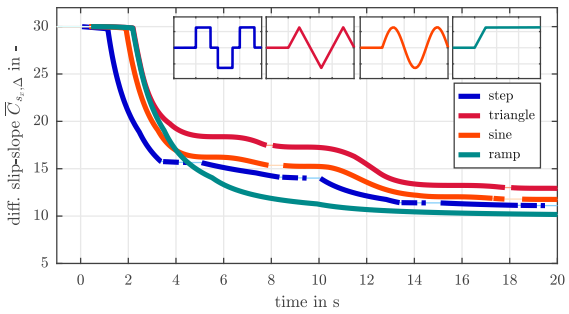

Figure 3.7.: Comparison of estimated slip slope time histories for different excitation functions from simulated signals: $A_{\text{exc}} = 250$ N, $a_x = 1$ m/s^2, $\tau = 10$ s, with activated minimum differential traction force coefficient criteria.

The plots in Figures 3.8a to 3.8d show the noise-free data points and their projections in the three-dimensional $s_{x,F}$-$s_{x,\Delta,F}$-$\mu_{\Delta,F}$ space with point size indicating the density of data points. The triangular, sinusoidal, and periodic ramp excitation functions have a continuous distribution of data points with the latter two having a slightly higher concentration at their minimum and maximum values, causing a slightly faster detection of a slip slope drop. The step function shows a concentration of data points around certain areas, especially at higher differential slips that allow fast detection and adaption to the slip slope values. The maximum excitation is reached immediately, but the discontinuous change of axle torques can be felt by the driver, increase loads on the drive train, and lead to tire forces exceeding the maximum friction potential.

Figure 3.9a (sine excitation, activated minimum $\mu_{\Delta,i}$ criteria) and 3.9b (triangular excitation, deactivated minimum $\mu_{\Delta,i}$ criteria) show comparisons of estimated slip slopes for different periods of the excitation function. Starting from the longest excitation period of 64 s the detection times decrease with shorter periods down to the minimum at 8 s. However, a further decrease in excitation periods causes an increase in the detection time again. For fast excitation frequencies, the differential slip increases rapidly at the beginning, but the total number of data points at high values is low since it is followed by a rapid decrease again. This causes the CUSUM to reach its threshold value later and therefore to a later detection of the slip slope change. When adjusting the CUSUM parameters the optimal excitation periods may change. For the simulated slip slope drop, the adaption time to the new slip slope value is similar for all excitation periods within the shown time.

Two different kinds of excitation amplitudes are compared in Figures 3.10a and 3.10b. For

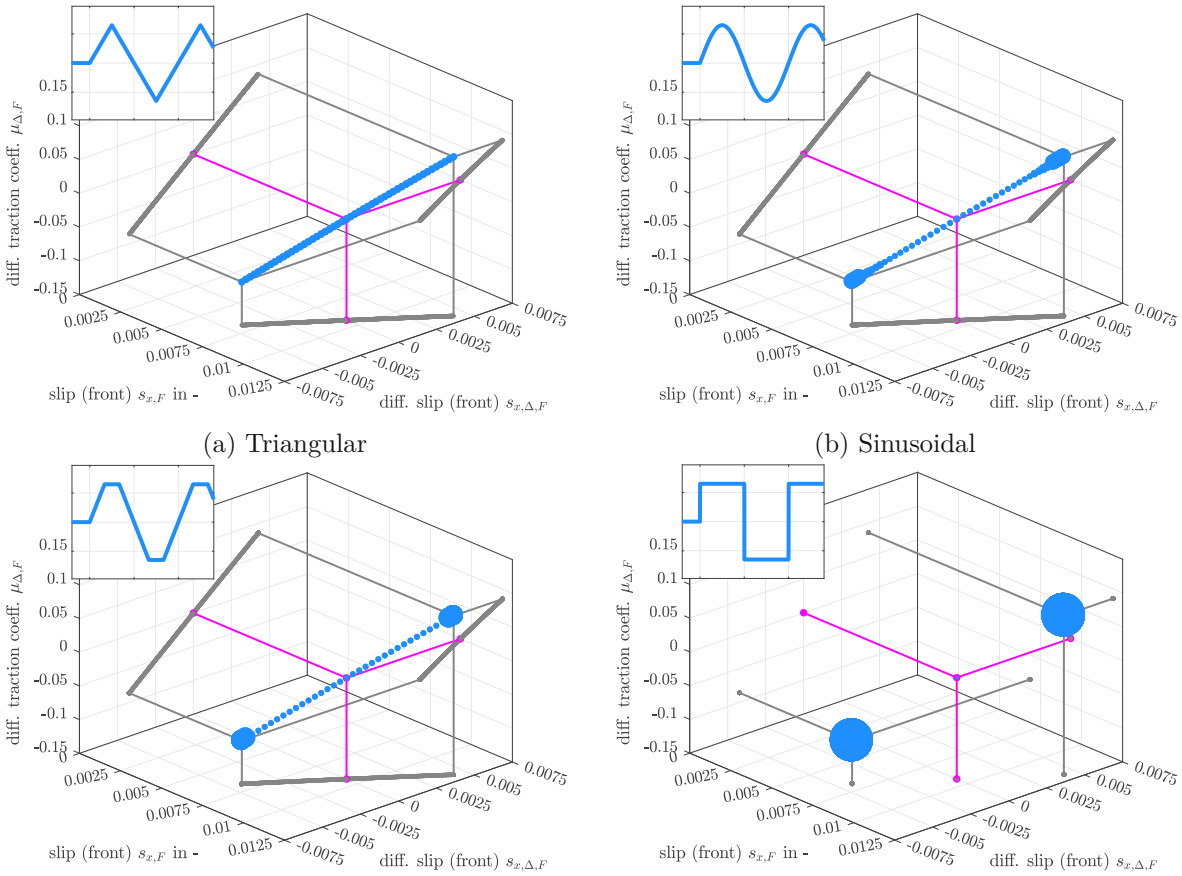

(a) Triangular (b) Sinusoidal

(c) Ramps (d) Steps

Figure 3.8.: Data points in $s_{x,F}$-$s_{x,\Delta,F}$-$\mu_{\Delta,F}$ plane for one period of different excitation functions with projections. The dot size indicates the local concentration of data points.

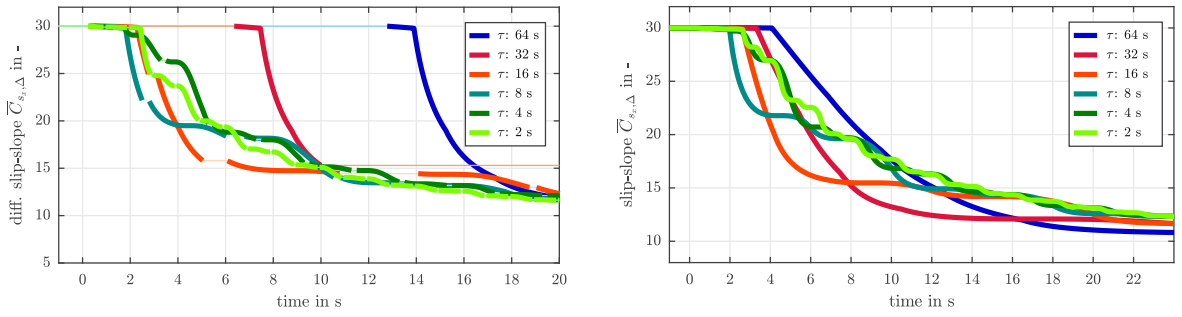

(a) Sine excitation function with minimum $\mu_{\Delta,i}$ criteria

(b) Triangular excitation function without minimum $\mu_{\Delta,i}$ criteria

Figure 3.9.: Comparison of estimated slip slope from simulated signals with a variation of excitation frequency: $A_{\text{exc}} = 250$ N, $a_x = 1$ m/s^2

relative amplitudes, Figure 3.10a, always positive axle forces are guaranteed. Detection of slip slope drops and adaption times to its new values are highly dependent on the amplitude (indicated by line color) but also on the current acceleration level (indicated

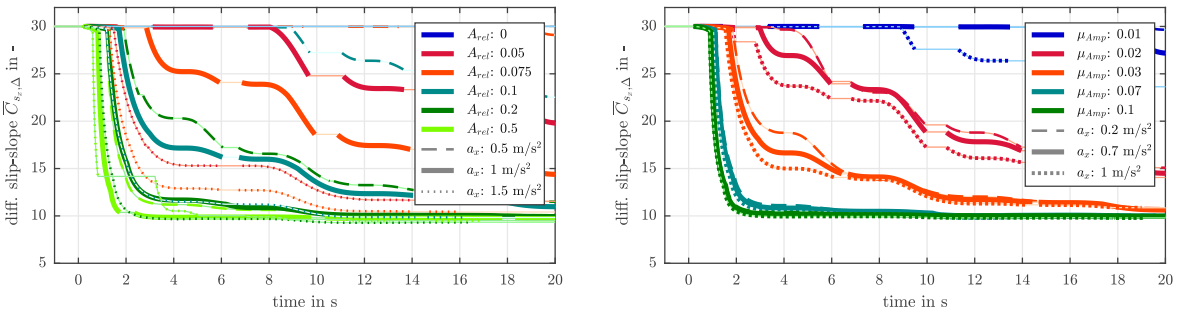

(a) Variation of the rel. excitation amplitude A_{rel}

(b) Variation of the traction force coefficient amplitude μ_{Amp}

Figure 3.10.: Time history of the estimated normalized slip slopes with a variation of the excitation amplitudes and acceleration levels a_x: $\tau_p = 8$ s, with minimum $\mu_{\Delta,i}$ criteria

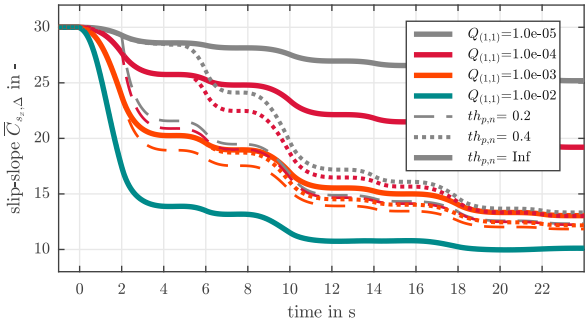

Figure 3.11.: Time history of the estimated normalized slip slopes with a variation of Kalman filter and CUSUM parameters for triangular excitation function, a_x: $\tau_p = 8$ s

by different line styles). If the excitation amplitudes are chosen as a fixed traction coefficient, Figure 3.10b, the estimator response is independent of current acceleration levels but may lead to negative forces on the wheels. Even very small traction coefficient amplitudes of $\mu_{\text{Amp}} = 0.03$ allow detection times of less than 2 s. With an amplitude of $\mu_{\text{Amp}} = 0.07$ the detection time is already just 1 s and the estimated slip slope decreases to almost real values within 2 s.

As indicated before, the Kalman filter and CUSUM parameters have a significant influence on detection times. In Figure 3.11 a comparison of the estimated slip slopes with different process covariance matrix entries $\mathbf{Q}_{(1,1)}$ and CUSUM thresholds $th_{p,n}$ is shown. These simulations were conducted to show the basic influence of these two parameters on the estimator behavior without noise and disturbances that occur in real-world measurements. The reset values of the state covariance matrix $\mathbf{P}$ were kept constant for this simulation.

Chapter 4

Scientific impact

This cumulative thesis describes **a new approach for pneumatic tire aquaplaning detection** using **a combination of known and novel criteria** for the detection of single aquaplaning effects using readily available signals in series production cars. These criteria allow both, a detection of full aquaplaning when tire-road contact is lost and large spin-ups or spin-downs occur, as well as partial aquaplaning forces are generated, the vehicle is still stable as well as controllable and a driver might not recognize upcoming aquaplaning.

A **systematic study of aquaplaning effects and the influence of relevant parameters** is conducted to identify limits for detection. Besides the main factors, longitudinal velocity and water depth, other parameters like tire inflation pressure, tire type, and wear are studied as they are relevant for the intensity or occurrence of the observed physical phenomena.

In addition to large spin-downs during full aquaplaning, short minor spin-downs were identified at velocities below, but close to full aquaplaning velocity. These allow early and unique identification of critical aquaplaning conditions on non-driven wheels, although they might not occur at all types of tires or water level heights.

Measurements of the slip slope decrease due to a reduction of contact patch length shows the theoretically described behavior for a wide range of parameters. The early drop of the initial slip slope allows the **identification of partial aquaplaning at velocities far below full aquaplaning speed**. However, summer tires with high inflation pressure show a relatively smaller reduction of the slip slope compared to low inflation pressures and new winter tires do not show any change of slip slope in the tested velocity ranges.

For practical slip slope estimation in all-wheel drive vehicles, **a novel slip slope estimation method** is introduced **without the need for the longitudinal velocity**

for the calculation of the longitudinal slip. It is based on differential measures of slip and traction coefficient between front and rear axle, instead of absolute slip based on longitudinal velocity. It allows the estimation for vehicles with different tire parameters on the front and rear axle and continuous adaption to its changes by estimation of a slip slope ratio parameter and tire radii ratio instead of absolute values. Therefore, the estimator can be parameterized for robustness against slow changes in vehicle parameters and high sensitivity to sudden road condition changes.

To further increase the availability of valid slip slope estimation and sensitivity to changes a novel **additional active tire force excitation** is proposed. The nominal traction forces are superimposed with an additional continuously changing force so that the resulting axle forces change from the nominal values. Their total sum is kept constant, ensuring vehicle velocity and acceleration are not changed from the values demanded by the driver or (semi-)autonomous system. This **variation causes a persistent excitation of slip and traction coefficient** parameters necessary for slip slope estimation. For situations with low traction demand, e.g. constant driving with low speed, it can be allowed that resulting axle forces become temporarily negative, e.g. through recuperation on electric vehicles, enabling sufficient levels of (differential) slip and traction force.

Based on the systematic study of aquaplaning phenomena and the novel slip slope estimator, single and combined phenomena methods for aquaplaning detection are developed. The joint detectors combine either the key criteria or the output of the single effect methods. The new methods allow the **detection of partial and full aquaplaning** in different driving situations and for different drivetrain concepts while still relying on measurement signals, which are already available in series production cars.

Paper I

Aquaplaning Detection Using Effect-Based Methods: An Approach Based on a Minimal Set of Sensors, Electronic Stability Control, and Drive Torques

Authors: Fichtinger, A., Edelmann, J., Plöchl, M., Höll, M.
Published in: IEEE Vehicular Technology Magazine, 16.3 (2021): 20-28.

Abstract: Knowledge of actual tire-road friction potential is most relevant for safe operation of automated vehicles and for adjusting advanced driver-assist systems. Aquaplaning may result in considerably reduced friction potential and unstable vehicle behavior for rear-wheel-drive vehicles; thus, awareness of risk of aquaplaning is crucial. Analysis of numerous measurements from driving on wet road surfaces, including, for example, different water levels, types of tires, tire inflation pressures, and tire wear, has revealed characteristic dynamic behavior of vehicles and their subsystems that could be related to an immediately approaching onset or the presence of aquaplaning. Thus, methods to detect such characteristic behavior are developed, and a combined detection algorithm based on effect-based criteria to detect the risk or presence of aquaplaning for rear-wheel-drive vehicles is proposed. The effectiveness and limitations of the individual methods, as well as the reliability of the presented algorithm, are shown based on measurements from test maneuvers.

Paper II

Pneumatic Tyre Aquaplaning: an Experimental Investigation on Manifestations and Influences of Appearance

Authors: Fichtinger, A., Bárdos, Á., Szalay, Z., Edelmann, J., Plöchl, M.
Published in: Acta Polytechnica Hungarica 19.9 (2022): 45-65.

Abstract: Aquaplaning at wet road conditions and high speeds can be a source of dangerous driving situations and accidents. The proper understanding of characteristic effects can be crucial in early aquaplaning detection and accident avoidance, essential for driver and driver assistance systems and trajectory planning for self-driving cars. Four test vehicles were equipped with a basic measurement system, and measurements were performed to evaluate characteristics of aquaplaning, such as wheel spin-up and wheel spin-down, change of rolling resistance, tyre slip slope, and tie rod force. Driveline configuration, type, wear and inflation pressure of the tyre(s), water level height next to chosen speed and performed manoeuvre significantly affect vehicle behaviour and thus the possibility to detect aquaplaning conditions. The results and main findings may allow and help establish corresponding methods to early detect aquaplaning and dangerous driving conditions.

Paper III

Slip slope change detection based on active drive force excitation

Authors: Fichtinger, A., Edelmann, J., Plöchl, M., Höll, M., Unterreiner, M.
Published in: Proceedings of the Institution of Mechanical Engineers. Part D, Journal of Automobile Engineering (2023), Web

Abstract: Identification of the available friction potential is crucial for road safety but difficult, in particular at normal driving. This paper aims to contribute by presenting an effect-based method for slip slope change detection related to friction potential changes at all wheel-drive vehicles applying active drive force excitation. The proposed estimation approach relies above all on the wheel speeds and the axle/wheel drive forces of the front and rear axle. Different types of periodic active drive force excitation that are superimposed to the drive force requested by the driver while maintaining the desired level of speed or acceleration are investigated w.r.t. the availability of the estimates and overall effectiveness of the estimator. Vehicle tests are performed to evaluate theoretical results and the (co-)driver's perception of the active drive force excitation. Results from both the simulation study and vehicle tests show that the proposed method allows to reliably estimate slip slope changes at all-wheel drive vehicles in driving conditions with low levels of drive force excitation.

Paper IV

Tire-Road Friction Potential Estimation for All-wheel Drive Vehicles with Active Longitudinal Tire Force Excitation

Authors: Fichtinger, A., Edelmann, J., Plöchl M.
Published in: In Proceedings of AVEC. Vol. 2022.

Abstract: The estimated slip-slope of the tires may be related to changed tire-road friction conditions. To improve the availability of the estimation and the sensitivity to changes of the road surface conditions of a 4WD vehicle, in this paper, an active force excitation method is proposed. Different excitation schemas will be discussed and compared. The effective drive force of the vehicle is not modified to maintain the acceleration/deceleration demands of the driver/driving robot.

Andreas Fichtinger

Expertise

Vehicle dynamics, multi body dynamics, state estimation, vibration technology, measuring technology

Skills

Languages
German, English, Polish, Spanish

Software/Coding
Matlab/SIMULINK, SIMPACK, Mathematica, SolidWorks, Java, ABAQUS, CATIA V5, Autodesk Inventor, LabVIEW, Python, C/C++, Visual Basic .NET, SQL

Education

TU Wien, Doctoral Program in Engineering Sciences, Vehicle Dynamics 2016 - 2024
Thesis: *Pneumatic tire aquaplaning detection using effect based methods with a minimal set of sensors*
supervised by Prof. Manfred Plöchl

TU Wien, Master Program Mechanical Engineering
2013 - 2015
Thesis: *Experimental and numerical study on the energy transfer in parametrically excited systems*
supervised by Prof. Horst Ecker

TU Wien, Bachelor Program Mechanical Engineering
2008 - 2013
Thesis: *Berechnung von Schwingungseigenschaften teilweise eingetauchter koaxialer Rohre*
supervised by Prof. Horst Ecker

HTBLuVA St. Pölten, Department of Informatics
2002 - 2007
Federal Higher Technical Institute for Education and Experimentation / Technical College

Experience

TU Wien, Institute of Mechanics and Mechatronics, Technical Dynamics and Vehicle Dynamics 2016 - 2022
Research Assistant

TU Wien, Institute of Mechanics and Mechatronics
2010 - 2015
Tutor in the courses: "Mechanics I & II", "Machine Dynamics", "Measuring and vibration technology"

SKF Steyr, Department Standard & Practices
Internship 2013

VOITH Paper, St. Pölten, Department for roll construction 2011
Internship